C 7 Polarization Handling: Synchrotron [1]

Shibabrata Nandi
Institut für Festkörperforschung
Forschungszentrum Jülich GmbH

Contents

[1] Lecture Notes of the 43rd IFF Spring School "Scattering Methods for Condensed Matter Research: Towards Novel Applications at Future Sources" (Forschungszentrum Jülich, 2012).

1 Introduction

Investigations of the structure and dynamics of materials have been an important and essential endeavor in condensed matter physics since the early 20^{th} century. Both neutron and x-ray scattering techniques have been used extensively to study the crystallographic structure of materials and provide complementary views of structure. For example, neutron scattering has traditionally been the standard tool for studies of magnetic structure and the dynamics of condensed matter systems. X-ray diffraction has largely been applied to detailed crystallographic structure determination. The principle interaction that makes structure determination possible for x-rays is the Coulomb interaction between x-rays and the electronic distribution which gives rise to driven harmonic oscillation of the electrons, and the emission of electric dipole radiation. This is the classical *Thomson scattering* process.

At x-ray absorption edges photoelectric absorption occurs and electrons are promoted from core levels into empty states above the Fermi level. Photons that take part in the photoelectric absorption are lost for the scattering experiment. However, the incident photons can also give rise to virtual transitions between core levels and states above the Fermi level that relax back to the core states with the emission of x-rays with the same energy as the initial beam. For charge scattering, this is known as *anomalous charge scattering* which yields additional terms in the x-ray scattering form factor that can be used to enhance the scattering contrast between neighboring elements. Anomalous scattering is also sensitive to the anisotropy of local environment, such as the arrangement of orbitals and orbital order. In addition to charge scattering, x-rays interact with the magnetic moment of the system. Indeed, the *magnetic scattering* of x-rays from electrons in molecules and solids is well documented in theory [1] and was observed experimentally by de Bergevin and Brunel in 1970's with a commercial x-ray tube [2]. de Bergevin and Brunel also presented a classical picture of the interaction between x-rays with electrons and magnetic moments [3] illustrated in Fig. 1. Unfortunately, from a practical point of view, the x-ray scattering cross-sections from electron spins are reduced by approximately six orders of magnitude compared to normal charge scattering and, therefore, using x-ray magnetic scattering to study magnetism was largely impractical in 1970's.

The situation changed in 1990's when Gibbs and coworkers successfully observed magnetic scattering from Ho metal due to the dramatic increase of photon flux available from synchrotron radiation.[4] The increased photon flux compensates for the weakness of the magnetic scattering signal. The polarization properties and tunability of the x-ray energy at a synchrotron source provides additional advantages for magnetic x-ray scattering. As will be discussed in the next section when x-ray energies are tuned through the absorption edges of an element of interest there is a resonant enhancement of the scattering signal now known as *x-ray resonant magnetic scattering* [5]. Away from the resonance condition, the magnetic scattering signal is known as *non-resonant x-ray magnetic scattering*. All of the above processes have been reviewed and described in detail in several texts [6, 7]. In the following, we will concentrate mainly on the basic principles and applications of the x-ray resonant magnetic scattering and nonresonant magnetic scattering.

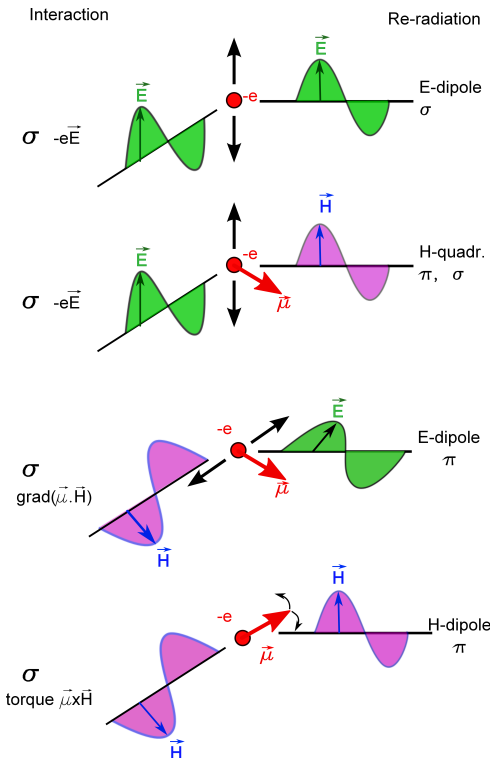

Figure 1: *Illustration of the processes leading to scattering of x-rays by the charge (top) and the spin moment (bottom three) of the electron in a classical picture. Figure has been adapted from de Bergevin and Brunel [3] and Th. Brückel [8].*

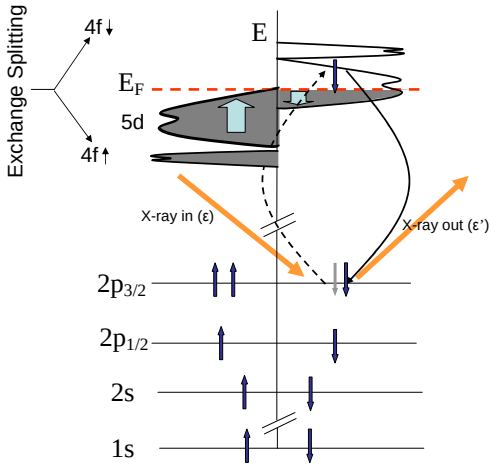

Figure 2: *Schematic illustration of the second order perturbation process leading to XRMS in the case of a lanthanide metal. An electron being photo-excited from the core level to the empty states above the Fermi energy E_F . The subsequent decay of the electron to the core level gives rise to an elastically scattered photon.*

2 Cross-section for the resonant and nonresonant magnetic x-ray scattering:

The calculation of the x-ray scattering cross-section from a quasi-relativistic Hamiltonian for a electron in a quantized electromagnetic field using second order perturbation theory was done by Blume [9] and Blume and Gibbs [10], and was later presented in a simplified form by Hill and McMorrow [11] in the coordinate system convenient for an x-ray resonant magnetic scattering experiment (XRMS) experiments. We start with the Hamiltonian for electrons in a quantized electromagnetic field:

$$\begin{aligned} H =& \sum_j \frac{1}{2m}\{\vec{P_j} - \frac{e}{c}\vec{A}(\vec{r}_{ij})\}^2 + \sum_{ij} V(\vec{r}_{ij}) - \frac{e\hbar}{2mc}\sum_j \vec{s}_j \cdot \nabla_j \times \vec{A}(\vec{r}_j) \\ & - \frac{e\hbar}{2(mc)^2}\sum_j \vec{s}_j \cdot \vec{E}(\vec{r}_j) \times \{\vec{p}_j - \frac{e}{c}\vec{A}(\vec{r}_j)\} + \sum_{\vec{k}\lambda} \hbar\omega_{\vec{k}}\{c^\dagger(\vec{k}\lambda)c(\vec{k}\lambda) + \frac{1}{2}\} \end{aligned} \tag{1}$$

Here, the first term corresponds to the kinetic energy of the electrons in the electromagnetic field, represented by the vector potential $\vec{\mathrm{A}}(\vec{\mathrm{r}})$. The second term corresponds to the Coulomb interaction between electrons, the third term corresponds to the Zeeman energy, $-\vec{\mu}\cdot\vec{H}$, of the electrons with spin $\vec{\mathrm{s}}_j$, the fourth term is the spin-orbit coupling in the initial or final states and the last term is the self energy of the electromagnetic field.
The vector potential $\vec{\mathrm{A}}(\vec{\mathrm{r}})$ is linear in photon creation and annihilation operator $c^\dagger(\vec{k}\lambda)$ and $c(\vec{k}\lambda)$, and can be expanded in plane wave form as:

$$\vec{A}(\vec{r}) = \sum_{\vec{q}\sigma}(\frac{2\pi\hbar c^2}{V\omega_q})^{\frac{1}{2}} \times [\vec{\epsilon}(\vec{q}\sigma)c(\vec{q}\sigma)e^{i\vec{q}\cdot\vec{r}} + \vec{\epsilon}^\star(\vec{q}\sigma)c^\dagger(\vec{q}\sigma)e^{-i\vec{q}\cdot\vec{r}}] \tag{2}$$

Here V is the quantization volume and $\epsilon(\vec{q}\sigma)$ is the unit polarization vector corresponding to a wave vector $\vec{q}$ and polarization state σ. The index $\sigma(=1,2)$ labels two polarizations for each wave vector $\vec{q}$. Since $\vec{\mathrm{A}}(\vec{\mathrm{r}})$ is linear in photon creation and annihilation operator, $c^\dagger(\vec{k}\lambda)$ and $c(\vec{k}\lambda)$, scattering occurs in second order for terms linear in $\vec{\mathrm{A}}$ and in first order for quadratic terms. For the spin orbit term in Eq. 1, $\vec{E}$ can be written in terms of scalar potential ϕ and the vector potential $\vec{A}$ as:

$$\vec{E} = -\nabla\phi - \frac{1}{c}\dot{\vec{A}} \tag{3}$$

After substituting $\vec{A}$ and $\vec{E}$ in Eq. 1, the Hamiltonian in Eq. 1 can be re-written as the sum of three terms:[9]

$$H = H_0 + H_R + H' \tag{4}$$

Where H_0 contains only the degrees of freedom for the electron system, H_R is the Hamiltonian for the quantized electromagnetic field and H' corresponds to the interaction between the electron and the radiation field. Scattering cross sections are calculated by assuming the solid is in a quantum state $|a\rangle$ which is an eigenstate of H_0 with energy E_0 and there is a single photon present. We then calculate the probability of a transition induced by the interaction term H' to a state $|b\rangle$, with photon $\vec{k}'\lambda'$. The transition probability (Ω) per unit time can be calculated using

"Fermi's golden rule" up to second order:

$$\Omega = \frac{2\pi}{\hbar}|\langle f|H^{'}|i\rangle + \sum_{n}\frac{\langle f|H^{'}|n\rangle\langle n|H^{'}|i\rangle}{E_i - E_f}|^2 \times \delta(E_i - E_f)$$
$$|i\rangle = |a;\vec{k}\lambda\rangle;\ |f\rangle = |b;\vec{k^{'}}\lambda^{'}\rangle \tag{5}$$

2.1 X-ray resonant magnetic scattering:

The cross-section for the elastic scattering can be written as:

$$\frac{d\sigma}{d\omega} = r_0^2\left|\sum_n e^{i\vec{Q}\cdot\vec{r_n}}f_n(\overrightarrow{k},\overrightarrow{k}',\hbar\omega)\right|$$

where, $d\sigma$ is the differential cross-section of scattering into the solid angle $d\omega$, $r_0 = \frac{e^2}{mc^2} = 2.8\times10^{-15}\,m$ is the classical electron radius, $\overrightarrow{Q} = \overrightarrow{k} - \overrightarrow{k}'$ is the momentum transfer, $\overrightarrow{k}$ and $\overrightarrow{k}'$ are the incident and scattered wave-vectors of the photon, f_n is the scattering amplitude of the nthatom which is at the position $\vec{r_n}$. While the detailed derivation of the scattering cross section is given in Ref. [9], we will outline here the final results. For coherent elastic scattering, ($|a\rangle = |b\rangle$), and the amplitude can be written as a sum over the following terms:[11]

$$f = f_0 + f^{'} + if^{''} + f_{spin} \tag{6}$$

Here, $f_0 \propto Zr_0$ is the Thompson charge scattering amplitude and f_{spin} is the non-resonant spin-dependent magnetic scattering amplitude. Far from resonance, $f^{'}$ and $f^{''}$ contribute terms proportional to the orbital and spin angular momentum. At resonance both electric and magnetic multipole transitions contribute through the terms $f^{'}$ and $f^{''}$. However, the electric dipole and quadrupole transitions are dominant with respect to magnetic multipole transitions by a factor of $\hbar\omega/mc^2$ ($\sim$ 60 for typical x-ray edges) and so the only electric multipole transitions will be considered here.
For the electric 2^L-pole resonance in a magnetic ion, the resonant contribution to the coherent scattering amplitude can be written as[12]

$$f^e_{EL}(\omega) = \frac{4\pi}{k}f_D\sum_{M=-L}^{L}[\hat{\epsilon}^{'\star}\cdot Y^{(e)}_{LM}(\hat{k}^{'})Y^{(e)\star}_{LM}(\hat{k})\cdot\hat{\epsilon}]F^e_{EL}(\omega) \tag{7}$$

Where $\hat{\epsilon}$ and $\hat{\epsilon}^{'\star}$ are the incident and scattered polarization vectors, and $\hat{k}$ and $\hat{k}^{'}$ are the incident and scattered wave vectors, respectively. $Y^{(e)}_{LM}(\hat{k})$ are the vector spherical harmonics and f_D is the Debye-Waller factor. The strength of the resonance is determined by the factor $F^e_{EL}(\omega)$, which is, to 0$^{\text{th}}$ order, determined by atomic properties:

$$F^e_{EL}(\omega) = \sum_{a,n}\frac{P_aP_a(n)\Gamma_x(aMn;EL)}{2(E_n - E_a - \hbar\omega - i\Gamma/2)} \tag{8}$$

Here, $|n\rangle$ is the excited state of the ion and $|a\rangle$ the initial state. P_a is the probability of the ion existing in the initial state $|a\rangle$ and $P_a(n)$ is the probability for a transition from $|a\rangle$ to an excited state $|n\rangle$. It is determined by overlap integrals between the two states $|a\rangle$ and $|n\rangle$. Γ_x and Γ are the partial line widths of the excited state due to a pure electric 2^L-pole (EL) radiative decay and

due to all processes, both radiative and non-radiative (including, for example, Auger decay), respectively. These electric multipole (predominantly dipole and quadrupole) transitions involve the virtual photo-excitation of an electron from a core level to the unoccupied states above the Fermi energy with a subsequent de-excitation to the core-levels yielding an elastically scattered photon. These processes become sensitive to the magnetic state in exchange split bands due to the difference in occupation of minority and majority bands as illustrated schematically in Fig. 2. Due to the resonant denominator in Eq. 8, enhancements occur at the absorption edges of the magnetic elements (e.g. when, E_n-$E_a = \hbar\omega$). The strengths of these enhancements for XRMS depend mainly on three factors as discussed by Hannon *et al.* [12] and shown by XRMS experiments on a series of rare-earth intermetallic compounds ($R\mathrm{Ni_2Ge_2}$, R= rare-earths) by Kim *et al.* [13]:

- The magnitude of the transition matrix element. Dipole transitions between states $|a\rangle$ and $|n\rangle$ differing in orbital angular momentum quantum number by ΔL = 1 are generally stronger than quadrupolar transitions with ΔL = 2. A large overlap of the wave functions $|a\rangle$ and $|n\rangle$ favors large transition matrix elements. In contrast, transitions from "s" core levels to "p" or "d" excited states do not show large resonance enhancements due to the small overlap of the wave functions.

- The difference in the density of empty states above the Fermi level for minority and majority spin states. To give an example: in lanthanide metals, the $5d$ bands are spin polarized due to the magnetic $4f$ states. However, the exchange splitting in the $5d$ is much weaker as compared to the $4f$ states and dipolar transitions $2p \rightarrow 5d$ are sometimes not much stronger than quadrupolar transitions $2p \rightarrow 5f$.

- The strength of the spin-orbit coupling in the ground and excited states. It is this coupling that provides electric multipole transitions with sensitivity to the spin magnetism.

Using the above-mentioned factors, we can qualitatively categorize the possible transitions according to the magnitude of the resonance enhancement, as listed in Table. 1.[8] Here we define the term "resonant enhancement" as the ratio between the intensity of magnetic Bragg peaks at the maximum of the resonance relative to the intensity for non-resonant magnetic scattering.
One of the strengths of resonant magnetic scattering is that the polarization state of the scattered x-rays can be modified with respect to that of the incident beam. Therefore, by analyzing the polarization of scattered x-rays, it is possible to discriminate between charge and magnetic scattering. Furthermore, by analyzing the intensity of scattered x-rays in different polarization channels, the spatial components of the ordered magnetic moment can be obtained.[14, 15] Therefore, in the following sections explicit relationship between the amplitude of scattered x-rays and incident x-rays will be shown according to Ref. [11].
For rare-earth L-edges, electric dipole transitions usually dominate the resonant magnetic cross section and are the simplest to calculate. An example of such a transition is the $2p_{3/2} \rightarrow 5d_{1/2}$ transition of Ho, which occurs at the L_{III} absorption edge. At this transition, the vector spherical harmonics can be written, for L = 1, M = $\pm$1:

$$[\hat{\epsilon}'^{\star} \cdot Y^{(e)}_{1\pm1}(\hat{k}')Y^{(e)\star}_{1\pm1}(\hat{k}) \cdot \hat{\epsilon}] = (3/16\pi)[\hat{\epsilon}' \cdot \hat{\epsilon} \mp i(\hat{\epsilon}' \times \hat{\epsilon}) \cdot \hat{z}_n - (\hat{\epsilon}' \cdot \hat{z}_n)(\hat{\epsilon} \cdot \hat{z}_n)] \tag{9}$$

Similarly, for L = 1, M = 0

$$[\hat{\epsilon}'^{\star} \cdot Y^{(e)}_{10}(\hat{k}')Y^{(e)\star}_{10}(\hat{k}) \cdot \hat{\epsilon}] = (3/8\pi)[(\hat{\epsilon}' \cdot \hat{z}_n)(\hat{\epsilon} \cdot \hat{z}_n)] \tag{10}$$

Table 1: *Magnitude of the resonance enhancement for XRMS for some elements relevant for magnetism. Only order of magnitude estimates are given with "weak" corresponding to a factor of about "10^0", "medium" to about "10^2" and "strong" to "$>10^3$" compared to the non-resonant magnetic scattering. After Ref. [66]*

Elements	Edge	Transition	Energy Range (keV)	Resonance Strength	Comment
$3d$	K	$1s \rightarrow 4p$	5-9	Weak	Small overlap
$3d$	L_I	$2s \rightarrow 3d$	0.5-1.2	Weak	Small overlap
$3d$	L_{II}, L_{III}	$2p \rightarrow 3d$	0.4-1.0	Strong	Dipolar, Large overlap, high spin polarization of $3d$
$4f$	K	$1s \rightarrow 4p$	40-63	Weak	Small Overlap
$4f$	L_I	$2s \rightarrow 5d$	6.5-11.0	Weak	Small overlap
$4f$	L_{II}, L_{III}	$2p \rightarrow 5d$, $2p \rightarrow 4f$	6.0-10.0	Medium	Dipolar and quadrupolar
$4f$	M_I	$3s \rightarrow 5p$	1.4-2.5	Weak	Small overlap
$4f$	M_{II}, M_{III}	$3p \rightarrow 5d$, $3p \rightarrow 4f$	1.3-2.2	Medium to strong	Dipolar, quadrupolar
$4f$	M_{IV}, M_V	$3d \rightarrow 4f$	0.9-1.6	Strong	Dipolar, large overlap, high spin polarization of $4f$
$5f$	M_{IV}, M_{II}	$3d \rightarrow 5f$	3.3-3.9	Strong	Dipolar, large overlap, high spin polarization of $5f$

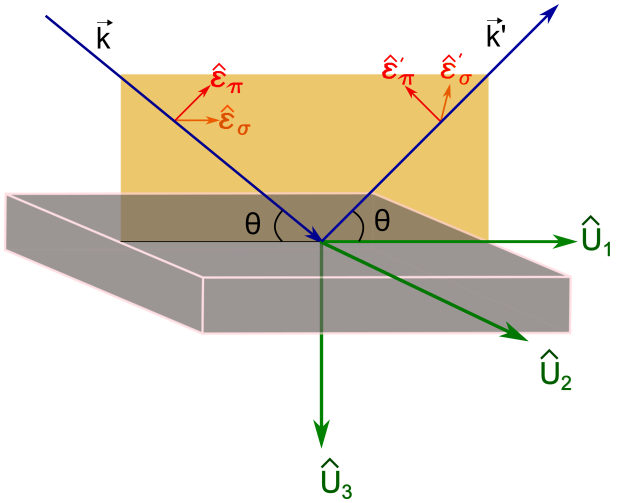

Figure 3: *The coordinate system used for the polarization dependence of the resonant scattering amplitudes described in the text. $\hat{k}$ and $\hat{k}'$ are the incident and scattered wave vectors and θ is the Bragg angle. $\hat{\epsilon}_\sigma$ ($\hat{\epsilon}'_\sigma$) and $\hat{\epsilon}_\pi$ ($\hat{\epsilon}'_\pi$) are the components of the polarization perpendicular and parallel to the scattering plane for incident (scattered) x-rays.*

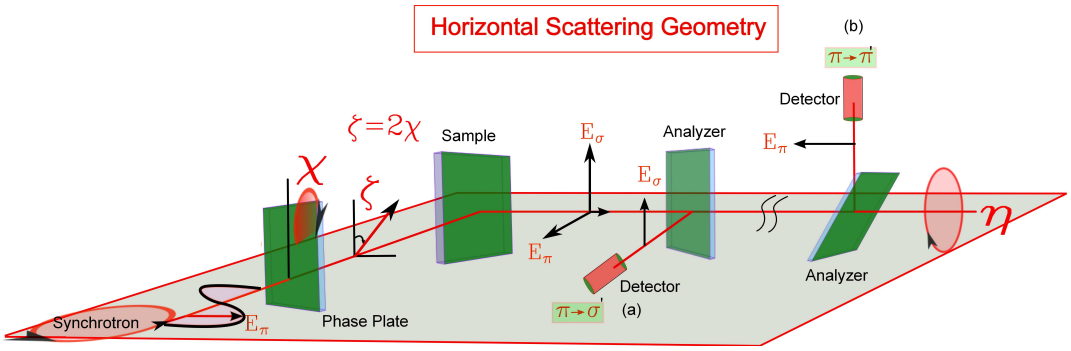

Figure 4: *Experimental realization of different polarization channels for the (a) $\pi \rightarrow \sigma'$ and (b) $\pi \rightarrow \pi'$ scattering geometries.*

where $\hat{z}_n$ is a unit vector in the direction of the magnetic moment of the nth ion. Thus,

$$f_{nE1}^{XRMS} = [(\hat{\epsilon}^{'} \cdot \hat{\epsilon})F^{(0)} - i(\hat{\epsilon}^{'} \cdot \times \hat{\epsilon}) \cdot F^{(1)} + (\hat{\epsilon}^{'} \cdot \hat{z}_n)(\hat{\epsilon} \cdot \hat{z}_n)F^{(2)}] \tag{11}$$

where $F^{(i)}$'s are the terms containing dipole matrix elements which have been evaluated by Hamrick for several rare-earths.[16] The first term of Eq. 11 contributes to the charge Bragg peak as it does not contain any dependence on the magnetic moment. The other two terms depend on the magnetic moment. All terms in Eq. 11 can be represented in 2×2 matrix form with polarization states chosen either parallel and perpendicular to the scattering plane and resolving each of the vectors $\hat{k}$, $\hat{k}^{'}$ and $\hat{z}_n$ into their components along the three orthogonal axes defined with respect to the diffraction plane shown in Fig. 3.

$$\begin{aligned} f_{nE1}^{XRMS} &= \begin{pmatrix} A_{\sigma\rightarrow\sigma'} & A_{\pi\rightarrow\sigma'} \\ A_{\sigma\rightarrow\pi'} & A_{\pi\rightarrow\pi'} \end{pmatrix} \\ &= F^{(0)} \begin{pmatrix} 1 & 0 \\ 0 & \cos 2\theta \end{pmatrix} - iF^{(1)} \begin{pmatrix} 0 & z_1 \cos\theta + z_3 \sin\theta \\ z_3 \sin\theta - z_1 \cos\theta & -z_2 \sin 2\theta \end{pmatrix} \\ &\quad + F^{(2)} \begin{pmatrix} z_2^2 & -z_2(z_1 \sin\theta - z_3 \cos\theta) \\ z_2(z_1 \sin\theta + z_3 \cos\theta) & -\cos^2\theta(z_1^2 \tan^2\theta + z_3^2) \end{pmatrix} \end{aligned}$$

Where $A_{\sigma\rightarrow\sigma'}$ represents scattering amplitude from the incident σ polarized x-rays to the scattered σ' polarized x-rays and so on.
The above matrix equation is sum of three sub-matrices: The first one contributes to the charge Bragg peak. The second and third contribute to the magnetic Bragg peak. A few points to note for the magnetic contribution:

1. The second term is linear in the components of the magnetic moment and therefore, mainly responsible for producing peaks at the magnetic wavevector, $\vec{\tau}$. For example, in an antiferromagnet with wavevector, $\vec{\tau}$, the linear term produces first harmonic satellite peaks. The third term, which is quadratic in the components of a magnetic moment produces second harmonic satellites as well as contributes to the charge Bragg peaks.[2] For a ferromagnetic material both the second and third term contribute to the positions of allowed charge reflections.

[2]for a commensurate antiferromagnet with propagation vector $\vec{\tau}$=0, it can produce intensity at the charge forbidden reciprocal lattice points.

2. Synchrotron radiation is linearly polarized in the plane of storage ring. Therefore, all combinations of polarization channels are accessible by suitably selecting the scattering plane (see Fig. 4 for experimental geometries) and, hence, different components of the ordered magnetic moment can be probed. For example, scattering in the $\sigma \rightarrow \pi^{'}$ channel is sensitive to the component of magnetic moment in the scattering plane (in the Fig. 3, z_1 and z_3) and $\pi \rightarrow \pi^{'}$ channel is sensitive to the components of a magnetic moment out of the scattering plane (z_2 in Fig. 3).

3. The scattering amplitude depends on the Bragg angle, and therefore by analyzing the magnetic peak intensities as a function of scattering angle, a specific magnetic model can be proved or disproved.

The scattering cross-section for the quadrupole transitions is much more complex and the reader is referred to the Ref. [17] for details.

2.2 Nonresonant x-ray magnetic scattering:

In many cases, the resonant process of XRMS is neither well understood nor efficient, especially at *K* edges for 3*d* transition metals. Nonresonant x-ray magnetic scattering (NRXMS) may be appropriate for these situations. The scattering amplitude of nonresonant x-ray magnetic scattering is directly related to the magnetic moment of the ions. While neutron scattering does not distinguish spin ($\vec{S}$) and orbital angular momentum ($\vec{L}$), $\vec{S}$ and $\vec{L}$ contribute differently to the scattering amplitude of the NRXMS. Far away from absorption edges of the all elements the scattering amplitude can be written as:[10]

$$f_n(\overrightarrow{Q}) = f_n^{charge}(\overrightarrow{Q}) + f_n^{NRXMS}(\overrightarrow{Q}, \overrightarrow{k}, \overrightarrow{k}')$$

In the limit of high photon energies, the nonresonant scattering amplitude may be written as

$$\begin{aligned} f_n^{NRXMS}(\overrightarrow{Q}) &= -i\frac{\hbar\omega}{mc^2}[\frac{1}{2}\overrightarrow{L_n}(\overrightarrow{Q}) \cdot \overrightarrow{A} + \overrightarrow{S_n}(\overrightarrow{Q}) \cdot \overrightarrow{B}] \\ &= -i\frac{\hbar\omega}{mc^2}\langle M_m \rangle \end{aligned} \tag{12}$$

Here $\overrightarrow{L_n}(\overrightarrow{Q})$ and $\overrightarrow{S_n}(\overrightarrow{Q})$ are the Fourier transforms of the orbital and spin magnetization densities, respectively. The vectors $\overrightarrow{A}$ and $\overrightarrow{B}$ contain different polarization and $\overrightarrow{Q}$ dependencies. Here the $\langle\rangle$ sign represent ground state expectation value of the operators. Due to this different $\overrightarrow{Q}$ and polarization dependencies in the nonresonant scattering amplitude, the orbital and spin components can be distinguished. This is in stark contrast to magnetic neutron scattering, where the scattering amplitude is sensitive to the sum of orbital and spin angular momentum. More explicitly, the expression for the neutron magnetic scattering can be written as:[9]

$$\langle M_n \rangle = \overrightarrow{Q} \times \{[\frac{1}{2}\overrightarrow{L_n}(\overrightarrow{Q}) + \overrightarrow{S_n}(\overrightarrow{Q})] \times \overrightarrow{Q}\} \cdot \overrightarrow{\sigma}$$

where $\overrightarrow{\sigma}$ is the neutron spin operator. For the point of view of performing synchrotron experiments, it is convenient to express $\langle M_m \rangle$ in a basis whose components are parallel and perpendicular to the scattering plane.

$$\begin{aligned}\langle M_m \rangle &= \begin{pmatrix} A_{\sigma\to\sigma'} & A_{\sigma\to\pi'} \\ A_{\pi\to\sigma'} & A_{\pi\to\pi'} \end{pmatrix} \\ &= \begin{pmatrix} \overrightarrow{S}\cdot(\hat{k}\times\hat{k}') & -\frac{Q^2}{2k^2}[\{\frac{\vec{L}(\vec{Q})}{2}+\overrightarrow{S}(\overrightarrow{Q})\}\cdot\hat{k}'+\frac{\vec{L}(\vec{Q})}{2}\cdot\hat{k}] \\ \frac{Q^2}{2k^2}[\{\frac{\vec{L}(\vec{Q})}{2}+\overrightarrow{S}(\overrightarrow{Q})\}\cdot\hat{k}'+\frac{\vec{L}(\vec{Q})}{2}\cdot\hat{k}'] & [\frac{Q^2}{2k^2}\overrightarrow{L}(\overrightarrow{Q})+\overrightarrow{S}(\overrightarrow{Q})]\cdot(\hat{k}\times\hat{k}') \end{pmatrix} \\ & \begin{pmatrix} (\sin 2\theta)S_2 & -2(\sin^2\theta)[(\cos\theta)(L_1+S_1)-(\sin\theta)S_3] \\ 2(\sin^2\theta)[(\cos\theta)(L_1+S_1)+(\sin\theta)S_3] & (\sin 2\theta)[2(\sin^2\theta)L_2+S_2] \end{pmatrix}\end{aligned}$$

Here we note that the diagonal elements are sensitive to the magnetization perpendicular to the scattering plane whereas the off-diagonal elements are sensitive to the magnetization within the scattering plane. Further, $\sigma \to \sigma'$ component is independent of orbital magnetization densities. In the same basis, the matrix describing the charge scattering can be written as:

$$\langle M_n \rangle = \rho(\overrightarrow{Q}) \begin{pmatrix} 1 & 0 \\ 0 & \cos 2\theta \end{pmatrix}$$

where $\rho(\overrightarrow{Q})$ is the Fourier transform of the electronic charge density.
Following Blume *et al*. [9] an estimate of the pure non resonant magnetic scattering strength compared to the charge scattering strength can be obtained as follows:

$$\frac{\sigma_{mag}}{\sigma_{charge}} = \left(\frac{\hbar\omega}{mc^2}\right)^2 \left(\frac{N_m}{N}\right)^2 \left(\frac{f_m}{f}\right)^2 \langle\mu^2\rangle$$

where $\frac{N_m}{N}$ is the ratio of the number of magnetic electrons compared to the total number of electrons, $\frac{f_m}{f}$ is the ratio between magnetic and charge form factors and $\langle\mu^2\rangle$ is the average value square of the magnetic moment. For Fe and 10 keV photons,

$$\frac{\sigma_{mag}}{\sigma_{charge}} \sim 4\times10^{-6}\langle\mu^2\rangle$$

Despite the smallness of the NRXMS compared to the charge scattering, NRXMS has been observed even for very small magnetic moment systems due to the intrinsic brilliance of the synchrotron radiation sources. [18, 19, 20, 21]

2.3 Examples of the resonance and the noresonance:

Before proceeding further, it is better to give real examples of resonant and nonresonant magnetic scattering. Figure 5 shows energy scans at the Sm L_2, L_3 and Fe K absorption edges for the compound SmFeAsO. Energy scans were performed at the magnetic Bragg positions of Sm (Fig. 5a & 5b) and Fe (Fig. 5c) moments, respectively. At 6 K (below the magnetic ordering temperature of Sm), at the Sm L_2 edge we observed a dipole resonance peak approximately 2 eV above the absorption edge for the (1 0 7.5) reflection. Similar energy scans were performed at the Sm L_3 edge and are shown in Fig. 5 (b). In addition to the dipole feature observed at the L_2 edge, a quadrupole feature appears approximately 6 eV below the Sm L_3 edge. Figure. 5(c) shows the energy scan through the Fe K-edge. Several features are observable in the energy spectrum: (a) Resonant features at and above E = 7.106 keV and (b) an energy independent non-resonant signal for energies below the resonant features. The non-resonant signal is about

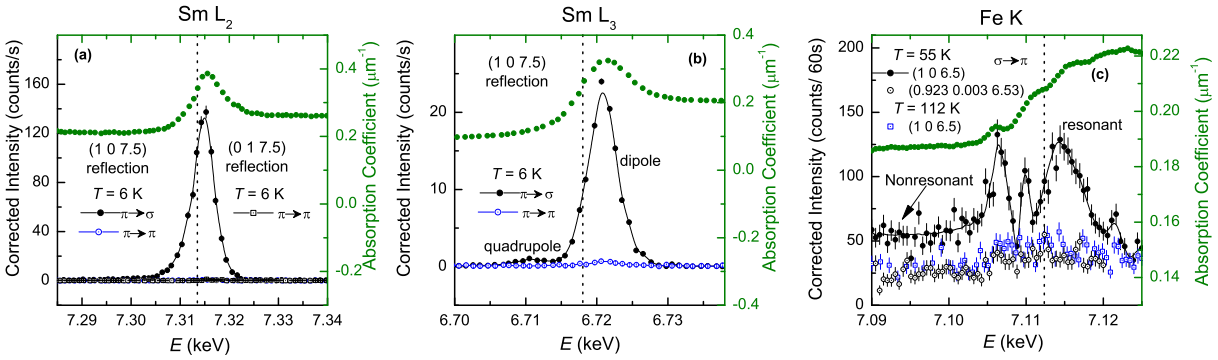

Figure 5: *(a,b) Energy scans of the (1 0 7.5) and (0 1 7.5) reflections and of the absorption coefficient at the Sm L_2 (left panel) and L_3 edges (middle panel). The dashed lines depict the Sm L_2 and L_3 absorption edges as determined from the inflection point of the absorption coefficient [22]. (c) Energy scans of the absorption coefficient and of the (1 0 6.5) reflection below (T = 55 K, filled circles) and above (T = 112 K, open squares) the magnetic ordering temperature of Fe moments and the measured background at T = 55 K away from the magnetic Bragg peak (open circles). The dashed line depicts the Fe K-edge. Both resonant and nonresonant signal can be clearly seen near the Fe K edge.*

a factor of 2.5 smaller than the resonant signal. To determine the polarization of the scattered x-rays, polarization analysis was performed using polarization analyzer which will discussed in more detail in section 4.4. Au (2 2 0) was used at Sm L_2 edge and Cu (2 2 0) was used for both the Sm L_3 and Fe K absorption edges as a polarization and energy analyzer to suppress the charge and fluorescence background relative to the magnetic scattering signal.

3 Poincaré Stokes Parameter:

To calculate the cross-section of magnetic scattering for any magnetic structure for an arbitrary incident polarization, it is convenient to introduce Poincaré representation for the the incident polarization and density matrix for the incident beam. In the co-ordinate system of non-resonant magnetic scattering amplitude the density matrix ρ can be written as:[10]

$$\rho = \frac{1}{2} \begin{pmatrix} 1+P_1 & P_2 - iP_3 \\ P_2 + iP_3 & 1-P_1 \end{pmatrix} \tag{13}$$

where $\vec{P} = (P_1,\ P_2,\ P_3)$ is the Poincaré-Stokes vector with components P_1, P_2, P_3. Taking $\hat{\epsilon}_\perp$ and $\hat{\epsilon}_{||}$ as two orthogonal unit vectors perpendicular and parallel to scattering plane (as in Fig. 3) we can write the incident electric field vector as:

$$\vec{E} = E_1\hat{\epsilon}_\perp + E_2\hat{\epsilon}_{||} \tag{14}$$

The components P_1, P_2, P_3 are defined as follows:

$$P_1 = \frac{|E_1|^2 - |E_2|^2}{|E_1|^2 + |E_2|^2} \quad (15)$$

$$P_2 = \frac{|E_1 + E_2|^2 - |E_1 - E_2|^2}{2(|E_1|^2 + |E_2|^2)} \quad (16)$$

$$P_3 = \frac{|E_1 + iE_2|^2 - |E_1 - iE_2|^2}{2(|E_1|^2 + |E_2|^2)} \quad (17)$$

P_1 = +1(-1) represent linear polarization along the $\hat{U}_2$ ($\hat{U}_3$) axis respectively. P_2 = +1(-1) represent linear polarization at an angle +45°(-45°) to the $\hat{U}_3$ axis, P_3 = +1(-1) represent left (right) circular polarization. If $\left|\vec{P}\right| = 1$, then the beam is completely polarized (100 %); $\left|\vec{P}\right| \leq 1$, the beam is partially polarized and for $\left|\vec{P}\right| = 0$, the beam is unpolarized. We should note that $\vec{P}$ is not a vector in real space, since it does not follow the transformation properties of a vector but can be thought of as vector in abstract space. If *M* represent the matrix for the scattering in the sample, then to calculate the density matrix and final polarization after scattering we need:

$$\vec{P} = tr(\sigma\vec{\rho}) \quad (18)$$

$$\rho' = M\rho M^\dagger \quad (19)$$

$$\frac{d\sigma}{d\omega} = \left(\frac{e^2}{mc^2}\right)^2 tr(\rho') \quad (20)$$

$$\vec{P'} = \frac{tr(\vec{\sigma}\rho')}{tr(\rho')} \quad (21)$$

where $\vec{\sigma}$ represents Pauli matrices. $\sigma_1 = \begin{pmatrix} 1 & 0 \\ 0 & -1 \end{pmatrix}$, $\sigma_2 = \begin{pmatrix} 0 & 1 \\ 1 & 0 \end{pmatrix}$, $\sigma_3 = \begin{pmatrix} 0 & -i \\ i & 0 \end{pmatrix}$ and $M^\dagger$ is the Hermitian conjugate of M.

4 Synchrotron instrumentation for the magnetic scattering:

For a magnetic scattering experiment we need a few basic components. (a) **The source**: From the discussion of the XRMS and NRXMS cross-sections, it is clear that for a successful magnetic scattering experiment one needs, polarized x-rays with high photon flux as well as tunability of the incident energy. Synchrotron radiation fulfills all the above criteria. (b) **The beamline**: This part prepares incoming x-ray from a synchrotron source for the experiment and consists of different optical elements such as monochromators (to change the wavelength of the incoming x-ray), focusing mirrors, slits (to define the beam cross-section), attenuators (to reduce the incident flux), and phase-plates (to change the incident polarization). All the optical elements are kept under vacuum and the beam is transported through evacuated tubes. (c) **The spectrometer**: For the observation of a diffraction peak, the sample has to be oriented within few tenths of a degree. This is done with a versatile diffractormeter with angular resolution better than 0.001°. A detector is attached with the 2θ arm and more often, before the detector a polarization analyzer is attached to analyze polarization of the scattered x-rays. (d) **Sample Environment**: Most of the cases, sample is placed in a cryostat to decrease the temperature of

the sample such that the sample is in a magnetically ordered state. This also allows measurement of magnetic order parameter as a function of temperature. Cryomagnets are used if one needs magnetic field for the experiment.

4.1 The source: synchrotron basics:

Here we will outline basic properties of synchrotron radiation relevant for the magnetic x-ray scattering. Basic electromagnetism tells us that an accelerating charge particle emits electromagnetic radiation. Synchrotron radiation occurs when an accelerating electrons or positrons follows a curved path in a relativistic speed. The electrons travel in a constant magnetic field which keep the electrons in a curved circular path.
Figure 6 shows the electron orbit in constant magnetic field. The direction of the radiation cone is in the direction of instantaneous velocity with opening angle ~$\gamma^{-1} = \frac{m_e c^2}{E_e}$ where $m_e c^2$ is the rest mass of an electron (= 0.511 MeV) and E_e is the energy of the circulating electrons. Typical energy E_e = 5 GeV of a third generation synchrotron radiation source gives the opening angle of the radiation cone $\gamma^{-1} \sim 0.1$ milli-radian. The synchrotron radiation is produced either in a bending magnet (BM) or some straight insertion devices are placed such as wigglers and undulators. The radiation coming out of a bending magnet is linearly polarized when viewed on axis. The beam is elliptically polarized above and below the axis with opposite helicities. The emitted radiation is very broad with emitted spectrum ranging from far-infra red to hard x-ray regime. However, the intensity of the emitted radiation falls of very rapidly for photon frequencies higher than $\gamma^3\omega_0$ where ω_0 is the angular frequency of an electron in the storage ring which is of the order of 10^6cycles/sec. Modern synchrotron radiation sources employ wiggler and undulators as insertion devices to increase the photon flux. These insertion devices consists of permanent magnets with opposite polls to create an alternating magnetic field perpendicular to the orbit of the storage ring. This alternating field leads to the sinusoidal movement of the charge particles withing the insertion devices. In an undulator or wiggler an important parameter characterizing the electron motion is the deflection parameter K given by: (see x-ray Data Booklet, http://xdb.lbl.gov/xdb-new.pdf)

$$K = \frac{eB_0}{2\pi m_e c} = 0.934\lambda_u[cm]B_0[T] \tag{22}$$

Where B_0 is the peak magnetic field and λ_u is the magnetic period. The maximum angular dispersion of the electrons in the orbit is given by $\delta = \frac{K}{\gamma}$. For an undulator, $K \lesssim 1$, and hence, the angular deviation is smaller than the opening of the radiation cone ($\sim \frac{1}{\gamma}$). Therefore, radiation from different poles adds coherently. The coherent addition of amplitude leads to monochromatic spectrum with odd harmonics on axis. Due to the finite number of magnetic poles the the radiation is quasi-monochromatic with a bandwidth of 0.1 %. The monochromaticity $\frac{\Delta\lambda}{\lambda}$ is inversely proportion to the number of polls and harmonics index number. For a wiggler, $K \gg 1(\sim 10)$, and the radiation from different polls adds incoherently.
The fundamental wavelength from an undulator radiation for an observation with an angle θ with the undulator axis is given by:

$$\lambda_1(\theta) = \frac{\lambda_u}{2\gamma^2}(1 + \frac{K^2}{2} + (\gamma\theta)^2) \tag{23}$$

Since $\lambda_u \sim 1$ cm and γ^{-2} is in the range 10^{-8}, the wavelength of the fundamental radiation lies in the Ångstrom range, i.e. in the x-ray regime. Furthermore, λ_1 can be varied by changing the

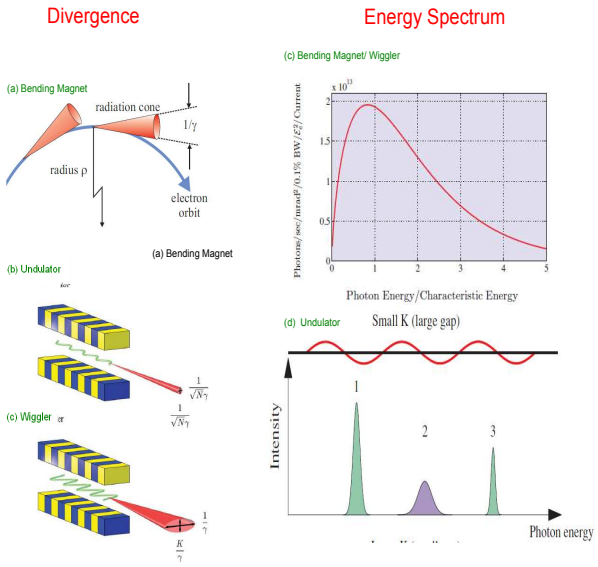

Figure 6: *(Left panel): Divergence properties synchrotron radiation of a Bending magnet, undulator and wiggler source. (Right panel): Energy spectrum from Bending magnet/wigglers and undulators. Figures taken from Ref. [23]*

magnetic field by varying the gap of the undulator (see. Eq. 22). The angular divergence of the undulator is substantially reduced compared to the bending magnet and the full width half maximum of the angular divergence is given by :[23]

$$\theta_{FWHM} \cong \frac{1}{\gamma}\sqrt{\frac{1+K^2/2}{nN}} \tag{24}$$

Where *n* is the harmonics index and *N* is the number of magnetic periods. This is much smaller than the angular divergence of the bending magnet which is $\sim \frac{1}{\gamma}$. The peak intensity of the undulator radiation scales with N^2 where as the central cone flux scales with N. Therefore, undulator radiation is highly collimated, linearly polarized in the plane, tunable with much improved flux which gives ideal condition for magnetic x-ray Scattering.

For the radiation from an wiggler, the radiated spectrum is same as that of a bending magnet with same filed strength, however with an intensity improved by a factor of 2N where N is the number of magnetic periods. The radiation is linearly polarized on-axis. However, off-axis polarization is still linear with different direction in compared with a bending magnet where off-axis polarization is elliptical. Divergence, energy spectrum and flux of the outcoming radiation from bending magnet (BM), undulators (ID) and wigglers has been compared in Fig. 6 and Fig. 7, respectively.

Worldwide, there exist four so-called "third generation synchrotron sources" for the hard x-ray regime: the European Synchrotron Radiation Facility ESRF in Grenoble, SPRING-8 in Japan, the Advanced Photon Source (APS) in Argonne, USA and the Petra III radiation source in Hasylab, DESY, Germany. All these facilities except ESRF have beamlines dedicated to magnetic scattering. The magnetic scattering beamline at ESRF has been recently closed after successful operation over years.

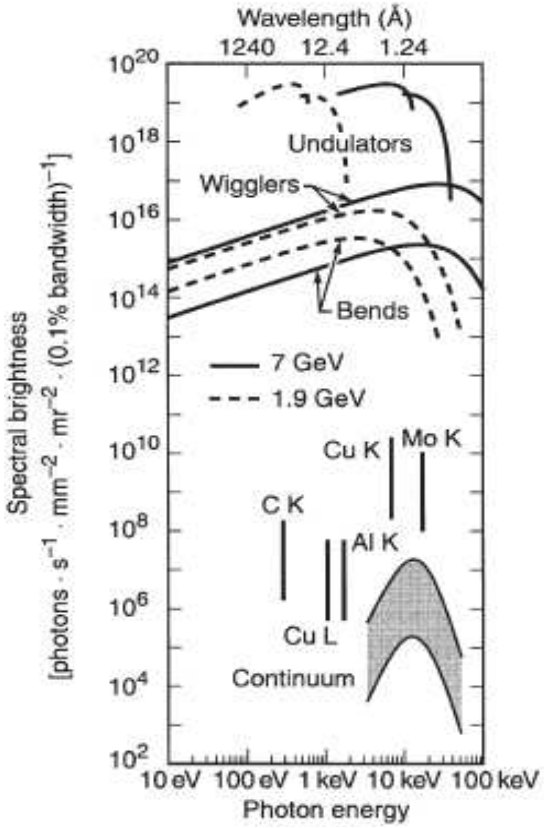

Figure 7: *Spectral brightness for the conventional laboratory x-ray tubes and several synchrotron radiation sources. The envelope of spectral brightness for today's third generation synchrotron facilities is somewhat higher than the curves above due to increased average beam current and decreased electron beam emmitance. Figure taken from x-ray data booklet.*

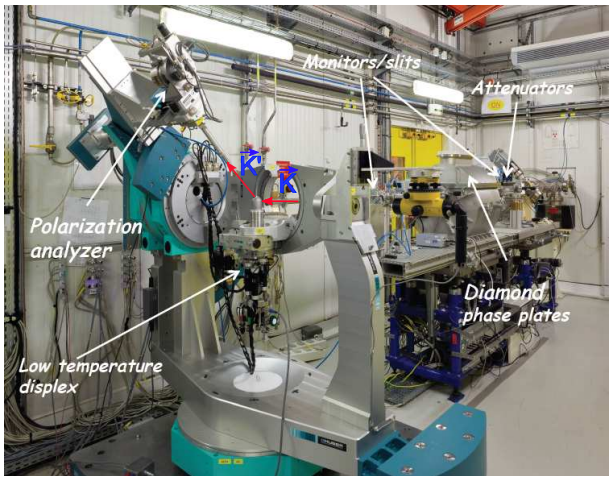

Figure 8: *Six-circle diffractometer at the ID20 beamline at ESRF, Grenoble.*

4.2 Beamlines:

The typical set-up of such a beamline is as follows: the beam from an undulator source is tailored by slit systems. Mirrors are used to suppress higher harmonics in the x-ray beam and/or to focus the beam onto the sample in the experimental hutch. The x-ray energy is selected by a double crystal Bragg monochromator. To handle the high heat load of several hundred W/mm^2, liquid nitrogen cooled silicon crystals are employed for monochromatization. Usually the Si (1 1 1) or Ge (1 1 1) reflection is chosen, since the second harmonic is largely suppressed for the Si crystal structure by the diamond glide planes. This beamline optics is situated in a so-called optics hutch with lead walls serving as biological radiation shielding. In the optics hutch, the x-ray beam is prepared with a desired properties and then enters the experimental hutch, where the actual scattering experiment is situated.

4.3 The Spectrometer:

Often, the six-circle diffractometers manufactured by Huber GmbH (http://www.xhuber.de) are used as a spectrometer. Figure 8 shows such a six circle diffractometer which was situated at the ID20 magnetic scattering bemline at ESRF. The diffractometer is equipped with a motorized analyzer stage and motorized translation stage. Motorized analyzer stage allows continuous rotation of the analyzer assembly around the scattered x-rays whereas motorized translation stage allows translation of the sample in three orthogonal directions. With this six circle diffractometer both the horizontal and vertical scattering planes can be utilized since the detector arm can be moved in the vertical direction as well as in the horizontal plane. Two types of detectors are generally used. The NaI photomultiplier tube and solid state detectors. NaI detectors has very low dark current ($\leq$0.1 counts/sec) and very high efficiency. However, it has very poor energy resolution.[24] On the other hand, solid state detectors have very high energy resolution which allows removal of fluorescence background with electronic discrimination.

4.4 Phase plate and the linear polarization analysis:

X-ray phase plates are used to manipulate polarization of the incident beam. One can change the direction of linear polarization using half wave plate and also, can convert linear polarization

into circular polarization using quarter-wave plates. Phase plates are based on the birefringence (anisotropy of refractive index) near Bragg-reflection. The component of transmitted electric field perpendicular (σ) and parallel (π) to the diffraction plane take a phase difference (Φ):[25]

$$\Phi = -\frac{\pi}{2}\frac{r_e^2\lambda^3 Re[F_h F_h^-]\sin(2\theta)t}{[\pi V^2]\Delta\Theta} \propto \frac{t}{\Delta\Theta} \tag{25}$$

where r_e is the classical electron radius, λ is the wavelength of the x-rays, t is the x-ray beam path in the crystal or the effective thickness, V is the volume of the unit cell, θ is the Bragg angle, F_h and $F_h^-$are the structure factors of the $(h\,k\,l)$ and $(\overline{h}\ \overline{k}\ \overline{l})$ reflections, respectively. The phase shift (Φ) is proportional to the effective thickness (t) of the crystal and inversely proportional to the angular offset ($\Delta\Theta$) from the Bragg peak. For a crystal with it's diffraction plane at an angle χ (see Fig. 4) and with a phase shift Φ, the Poincaré Stokes parameters are given by: [26]

$$P_1 = 1 + [\cos\Phi - 1]\sin^2 2\chi \tag{26}$$

$$P_2 = \sin^2\frac{\Phi}{2}\sin(4\chi) \tag{27}$$

$$P_3 = -\sin\Phi\sin(2\chi) \tag{28}$$

For $\Phi = \pm\frac{\pi}{2}$ and $\chi = 45^\circ$, the linear components P_1 and P_2 are zero whereas the circular component $P_3 = \pm 1$. This is known as Quarter Wave Plate (QWP) in optics which produces circularly polarized light from an incident linear polarization. The sign of the phase shift determines the helicity of the circular polarization, i. e. left or right circular polarization. If $\Phi = \pm n\pi\,(n = 0, \pm 1, \pm 2, ...)$, the the circular component is zero and the two linear components are given by: $P_1 = \cos(4\chi)$ and $P_2 = \sin(4\chi)$. This is known as Half Wave Plate (HWP). Variation of P_1 and P_3 as function of offset angle $\Delta\Theta$ for (1 1 1) diamond plate is shown in Fig. 9.

The polarization state of the scattered beam or the direct beam can be analyzed using a linear polarization analyzer (PA). A polarization analyzer is based on Thomson charge scattering from crystal such that the scattering angle (2θ) is close to 90°. The condition $2\theta = 90^\circ$ is fulfilled only approximately as a perfect mach of polarization analyzer crystal d spacing with the incident x-ray energy can not always be obtained. A list of different PA crystals in different energy range is listed in Table. 2. The intensity of the scattered radiation from an analyzer crystal can be written as:

$$I = \frac{I_0}{2}[1 + P_1\cos(2\eta) + P_2\sin(2\eta)] \tag{29}$$

where η is the rotation angle of the PA around the beam axis (see Fig. 4).

As an example, let us analyze the polarization of the direct beam with a Au(1 1 1) analyzer crystal. The energy is chosen such that $2\theta_P = 90^\circ$ condition is fulfilled. In this case, the polarization of the direct beam has been changed using a HWP by changing χ of the diamond phase plate. The rotation of incident light (ζ) is related to the rotation angle of diamond phase plate by : $\zeta = 2\chi$ (see Fig. 4). The integrated intensity of the scattered beam from the PA has been measured as function of η by rocking the analyzer crystal for a particular ζ and is plotted for different values of ζ in Fig. 10. The curves for a particular ζ has been fit with Eq. 29 and the values of P_1 and P_2 are extracted. These procedure is followed with different ζ and the

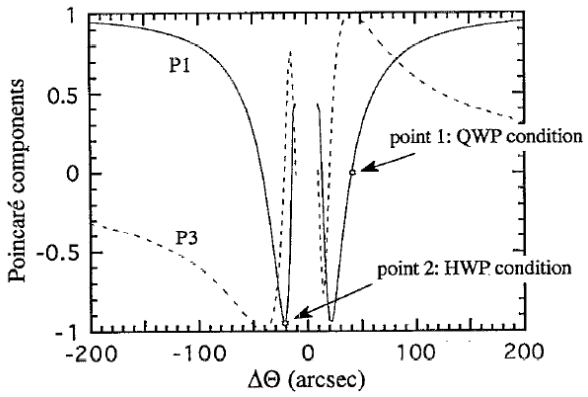

Figure 9: *Poincaré components (P_1 and P_3) as a function of offset angle $\Delta\Theta$ for a (1 1 1) diamond phase plate with 0.77 mm thickness in an (1 1 $\bar{1}$) asymmetric Laue geometry (beam path of 0.99 mm). Figure taken from Ref. [25]*

.

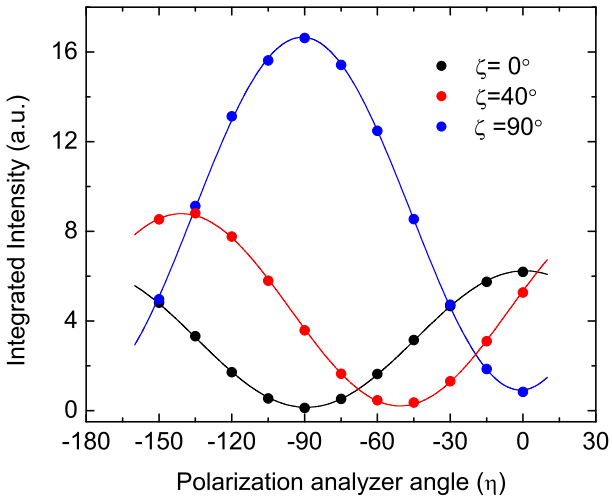

Figure 10: *Polarization analyzer angle (η) dependence of the scattered intensity for different incident linear polarization. The solid lines are the fits using Eq. 29 to extract Poincaré Stokes parameters.*

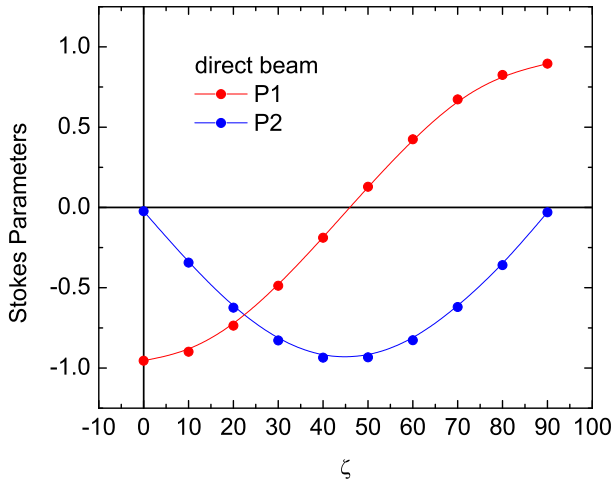

Figure 11: *Poincaré-Stokes parameters for direct-beam from a phase plate as a function of rotation of the incident light polarization.*

resulting values of P_1 and P_2 are plotted as a function of ζ in Fig. 11. The variation of P_1 and P_2 follows the theoretical prediction $P_1 = \cos(4\chi)$ and $P_2 = \sin(4\chi)$. Note that the degree of circular polarization can not be determined in this way. However an upper limit can be placed since $P_3^2 \leq 1 - P_1^2 - P_2^2$.

It is also possible to determine P_1 and P_2 by collecting integrated intensities for a pair of η values since P_1 and P_2 can be written from Eq. 29 as $P_1 = [I(0°) - I(90°)]/[I(0°) + I(90°)]$ and $P_2 = [I(+45°) - I(-45°)]/[I(+45°) + I(-45°)]$. However, it is recommended to measure integrated intensity at different positions of η with step size of minimum 30° between 0° and 180° to estimate the systematic error [27]. Furthermore, the integrated intensities should be measured by rocking the analyzer crystal to avoid the artifacts from the variable resolution function as a function of η.

There are several benefits of using polarization analyzer. PA analyzer reduces the background signal from fluorescence and diffuse signal. It also reduces the remaining higher harmonics.

5 Applications of the magnetic x-ray scattering:

X-ray magnetic scattering have many applications ranging from the study of the thin film magnetic system to the magnetism of bulk. Here few examples are selected to illustrate the power and versatility of the resonant and nonresonant magnetic scattering.

5.1 Determination of moment direction:

For a magnetic structure determination a basic and first step is to determine the direction of magnetic moments within the unit cell. In different ways this can be done, viz. (a) azimuthal rotation (b) Q-dependent measurements (c) by analyzing Poincaré Stokes parameters of the scattered beam. We will discuss all the procedures in the following sections with examples selected from different compounds with present relevance.

Table 2: *A list of analyzer crystals which are commonly used for polarization analysis. The photon energy for $2\theta_{PA} = 90^\circ$ is presented in columns 3 and 6. PG stands for Pyrolytic graphite.*

Crystal	(H K L)	*E* (90°) [keV]	Crystal	(H K L)	*E* (90°) [keV]
Au	(1 1 1)	3.73	Pt	(2 2 0)	7.74
Al	(1 1 1)	3.75	PG	(0 0 6)	7.84
LiF	(2 0 0)	4.35	Ge	(3 3 3)	8.05
Cu	(2 0 0)	4.85	Si	(3 3 3)	8.39
PG	(0 0 4)	5.22	Cu	(2 2 2)	8.41
Mo	(2 0 0)	5.57	LiF	(4 0 0)	8.71
Al	(2 2 0)	6.12	Pt	(4 0 0)	8.94
LiF	(2 2 0)	6.16	Pd	(4 0 0)	9.01
Cu	(2 2 0)	6.86	Cu	(4 0 0)	9.70
Au	(2 2 2)	7.44	PG	(0 0 8)	10.48
Al	(2 2 2)	7.49	Au	(3 3 3)	11.16

Azimuthal angle dependence:

$Gd_5(Si_xGe_{1-x})_4$ have received attention due to their magnetocaloric, magnetostrictive and magnetoresistive properties [28, 29, 30, 31]. Tan *et al.* [32] have undertaken determination of magnetic structure of the Gd moments in Gd_5Ge_4 using XRMS at the Gd L_{II} edge. Since naturally occurring Gd is strongly neutron absorbing, XRMS is a feasible option to determine the magnetic structure of this compound.

Magnetization measurement indicate that the Gd_5Ge_4orders antiferromagnetically below T_N = 127 K. Also, the measurements of magnetic susceptibility along three crystallographic directions indicate that the moment is along the *c* direction. Therefore, the crystal was mounted with *b* axis vertical and the *c* and *a* axis in the horizontal plane. The magnetic (0 3 0) reflection was accessed. In this geometry the crystal can be rotated around the $\vec{Q} = (0\,3\,0)$ such that the angle ψ between the *c* axis and the scattering plane can be continuously changed from 0° to 180°. The rotation of crystal around a scattering vector without changing value of Q vector is know as azimuthal rotation. A cartoon of azimuthal rotation is shown in Fig. 12.

By rotating the crystal around the *b* axis either *b*-*c* or *a*-*b* can be brought into the scattering plane. The integrated intensity of the (0 3 0) magnetic peak was collected as a function of ψ and was normalized to the charge (0 4 0) reflection for every azimuth angle to reduce the systematic error and is shown in Fig. 13. The dipole scattering intensity is sensitive only to the moment in the scattering plane with a cross section $f \propto \hat{k'}\cdot\hat{\mu}$ ($\hat{k'}$ and $\hat{\mu}$ are the wave vectors of the scattered photon and the magnetic moment respectively.) With $\psi = 90^\circ$ (a-b in the scattering plane), the integrated intensity is close to zero. Whereas when $\psi = 90^\circ$ or 180° (*b*-*c* in the scattering plane), the integrated intensity is maximum. Therefore, only *c* component of the magnetic moment contributes to the resonant scattering. Let us assume that the moments are at an angle ψ_c with respect to the *c* axis. Then the angle between the magnetic moment and the scattering plane for an azimuth angle ψ (defined as the angle between *c* axis and the scattering plane) is equal to $(\psi - \psi_c)$. Therefore, $f \propto \cos(\psi - \psi_c)$ and the integrated intensity can be written as $I = A\cos^2(\psi - \psi_c)$ where *A* is an arbitrary scaling factor. The solid line in Fig. 13

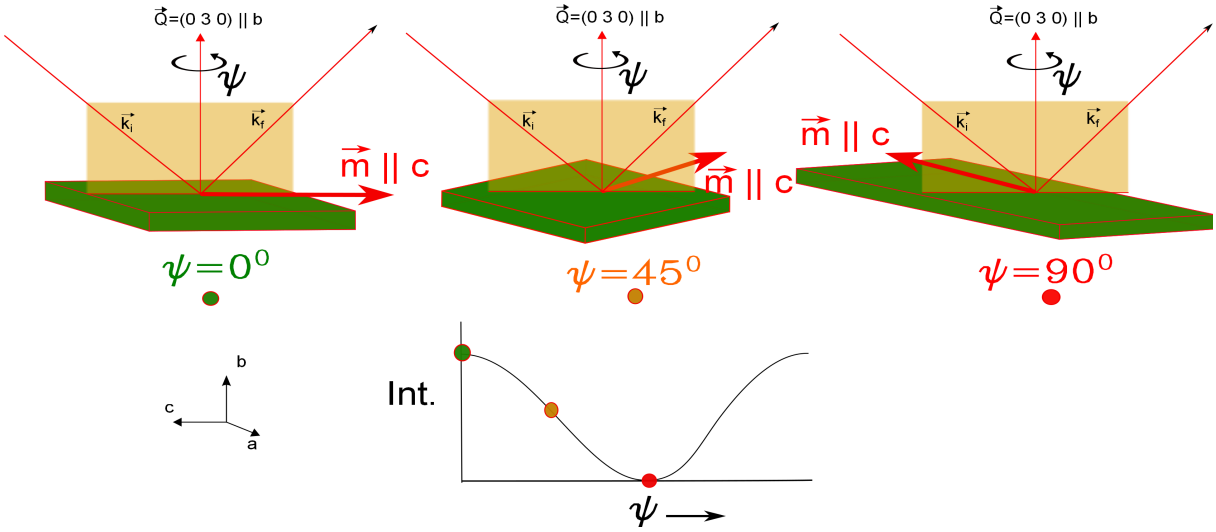

Figure 12: *Schematic representation of the azimuthal rotation. The ψ angle is defined as the angle between the crystallographic* c *axis and the scattering plane. When* c *axis lies within the scattering plane, ψ is defined as zero. When ψ = 90°, the* c *axis is perpendicular to the scattering plane. Expected variation of the dipole resonance intensity for the magnetic moment along the* c *direction.*

represents a fit with the above equation with $\psi_c = 1.9° \pm 1.8°$. Therefore, the magnetic intensity to the (0 3 0) reflection is sensitive only to the moment along *c* direction and indicate that either there is no magnetic component along *a* or *b* axis or the intensity of the (0 3 0) magnetic peak is not sensitive to either the *a* or *b* magnetic components due to cancellations arising from the symmetry of the magnetic order. Later, it was verified by a detailed Q-dependent measurements that the magnetic moments are indeed along the *c* direction.

One may note that the integrated intensity at $\psi = 0°$ deviates significantly from the calculated curve. This is due to the presence of multiple charge scattering. [33] Multiple charge scattering is particularly a problem for commensurate magnetic structures. Multiple charge scattering arises due to two or more successive Thompson scattering events. It occurs when another lattice point $\vec{Q}_2$ (secondary reflection) intercept the Ewald sphere other than the lattice point of interest $\vec{Q}_1$ (primary reflection). A third reflection $\vec{Q}_3 = \vec{Q}_1 - \vec{Q}_2$ is required to bring the secondary reflection into the direction of main reflection. In this case, not only $\vec{Q}_1$ but also $\vec{Q}_2 + \vec{Q}_3$ contribute to the observed intensity. Multiple diffraction depends on several factors such as incident energy of the x-rays, azimuth angle and crystal symmetry, lattice constants etc. For a resonant magnetic scattering experiment resonance occurs at particular energy or within a very small energy range. Therefore, one can reduce the multiple charge scattering background by varying the azimuth angle (rotation around the primary reflection $\vec{Q}_1$) such that $\vec{Q}_2$ is out of the Bragg condition. Typically a very small rotation ($\leq 1°$) is needed. The problem of multiple charge scattering becomes severe for high energy magnetic diffraction since size of the Ewald sphere is larger and correspondingly, more and more secondary reflection can intercept the Ewald sphere. In practice, energy scans around the resonant energy as a function of azimuth angle is performed to select multiple charge scattering free region. Fig. 14 (a) shows contour map of intensity in dependence on energy and azimuth angle for the (5 0 0) reflection. The multiple scattering contribution at the resonant energy can be minimized through a judicious choice of azimuth angle as shown in Fig. 14 (b), where the resonant scattering is well separated

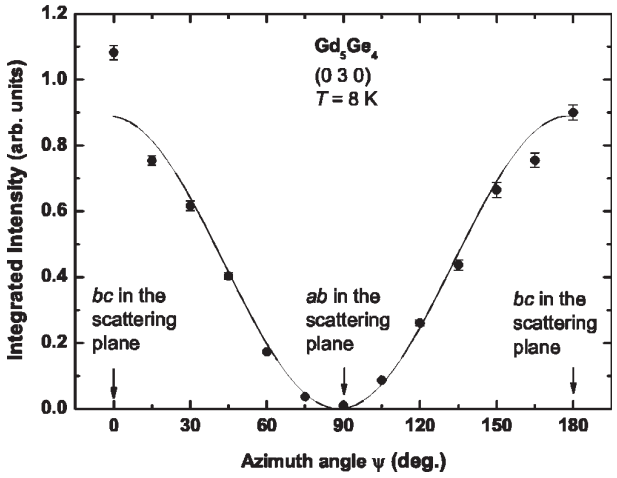

Figure 13: *The integrated intensity of the (0 3 0) magnetic peak normalized by the (0 4 0) charge peak at T = 8 K. The solid curve represents the variation expected for magnetic moments along the c axis. The Figure has been taken from Ref.[32].*

from the multiple scattering.

Q-dependence:

The conventional way to determine the moment direction is to measure the scattered intensity as a function of scattering angle which is commonly known as "Q dependent" measurement in the scattering community. There are many examples of using this procedure to determine the moment direction and magnetic structure [15, 14]. Here we will present the case of SmFeAsO [34]. SmFeAsO is the parent compound for the recently discovered superconducting $SmFeAsO_{1-x}F_x$ compounds where the highest T_c of 55 K has been observed. [35, 36]

SmFeAsO crystallizes in the tetragonal $P4/nmm$ space group and undergoes a structural phase to an orthorhombic crystal structure $Cmme$ below T_S = 140±1 K. Below T_{N1} = 110 K, a magnetic signal was observed at the reciprocal lattice points characterized by the propagation vector $(1\,0\,\frac{1}{2})$ when the x-ray energy was tuned through the Sm L_2 and Fe K-edges, indicating the onset of Sm and Fe magnetic order, respectively.

For the determination of the magnetic structure in the temperature range $5\,K \leq T \leq 110\,K$, one has to look into the details of the magnetic structures allowed by the space group symmetry and the propagation vector $(1\,0\,\frac{1}{2})$. Six independent magnetic representations (MRs) are possible [38]. All the MRs along with the calculated intensities for different polarization geometries are listed in Table 3 . For a second-order phase transition, Landau theory predicts that only one of the six above mentioned MRs is realized at the phase transition [38]. We note that the $\pi \rightarrow \pi'$ scattering geometry is sensitive only to the moment perpendicular to the scattering plane for the dipole resonance . Since, no magnetic signal was observed at the (0 1 7.5) (sensitive to Γ_1 and Γ_8) and (1 0 7.5) (sensitive to Γ_2 and Γ_7) reflections in the $\pi \rightarrow \pi'$ scattering channel at the Sm L_2 edge, one can exclude the moment in the a and b directions and hence, the MRs Γ_1, Γ_8, Γ_2 and Γ_7. To differentiate between the MRs Γ_4 and Γ_5 (moment along the c direction), the integrated intensities for a series of $(1\,0\,\frac{L}{2})$ reflections were measured, see Fig. 15(a).

To differentiate between these two MRs, angular dependence of the magnetic scattering has

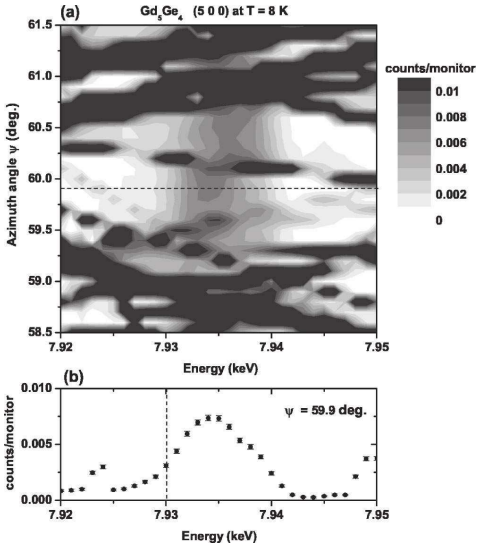

Figure 14: *(a) Contour map of the intensity as a function of energy and azimuth angle ψ at the (5 0 0) position and T = 8 K. Discontinuities in the bands of multiple scattering across the energy range are artifacts of the scanning process and (b) single energy scan at the azimuth angle* c *= 59.9°, which is depicted as a horizontal dashed line in (a). In (b), the vertical dashed line represents the position of the Gd L_{II} absorption edge. Figure adapted from Ref. [32].*

been calculated as outlined below. The intensity for a particular reflection can be written as:

$$I = SAL|F_m|^2 \tag{30}$$

where *S* is arbitrary scaling factor, $A = \frac{\sin(\theta+\alpha)}{\sin\theta\cos\alpha}$ is the absorption correction, $L = \frac{1}{\sin 2\theta}$ is the Lorentz factor. $|F_m|$ is the modulus of the magnetic structure factor. The magnetic structure factor F_m for the (*h k l*) reflections can be written as:

$$F_m = \sum_j f_j e^{2\pi i(hx_j+ky_j+lz_j)} \tag{31}$$

The summation is over all the magnetic atoms in the unit cell. f_j is the resonant/non-resonant magnetic scattering amplitude. The angular dependence of the magnetic structure factor comes from the magnetic scattering amplitude (f_j). For dipole resonance and for the $\pi \rightarrow \sigma$ geometry $f \propto \hat{k_i}\cdot\hat{\mu}$ where $\hat{k_i}$ and $\hat{\mu}$ are the wave vectors of the incoming photons and the magnetic moment, respectively. Here, α is the angle that the scattering vector $\vec{Q}$ (= $\vec{k_f}$-$\vec{k_i}$) makes with the crystallographic *c* direction perpendicular to the surface of the sample and, θ is half of the scattering angle. α is positive/negative for larger/smaller angles for the outgoing beam with respect to the sample surface. For the dipole resonance, and for the reflections of the type $(1\,0\,\frac{L}{2})$, $|F_m|^2$ is proportional to $\sin^2(2\pi zL)\sin^2(\theta+\alpha)$ and $\cos^2(2\pi zL)\sin^2(\theta+\alpha)$ for the Γ_4 and Γ_5 MRs, respectively. $z = 0.137$ is atomic position of Sm moments within the unit cell [37]. While $\sin^2(2\pi zL)/\cos^2(2\pi zL)$ term comes from the relative orientation of the magnetic moment within the magnetic unit cell, the term $\sin^2(\theta+\alpha)$ comes from the dot product between $\vec{k_i}$ and $\hat{\mu}$ [$(90^\circ - \theta - \alpha)$ is the angle between $\hat{k_i}$ and $\hat{\mu}$].

We note, that there is only one free parameter for the dipole intensity (see Eq. 30), namely the arbitrary scaling factor S. Figure 15(a) shows a fit to the observed intensities for the two above mentioned MRs. Since the model calculation with the magnetic moment in the Γ_5 MR closely

Table 3: *Basis vectors for the space group* $Cmme$ *with* $\mathbf{k}_{17} = (0,\ 1,\ .5)$. *The decomposition of the magnetic representation for the* Sm *site* $(0,\ .25,\ .137)$ *is* $\Gamma_{Mag} = 1\Gamma_1^1 + 1\Gamma_2^1 + 0\Gamma_3^1 + 1\Gamma_4^1 + 1\Gamma_5^1 + 0\Gamma_6^1 + 1\Gamma_7^1 + 1\Gamma_8^1$. *The atoms of the nonprimitive basis are defined according to 1:* $(0,\ .25,\ .137)$, *2:* $(0,\ .75,\ .863)$. *Lattice parameters of the orthorhombic crystal at 100 K [37]:* $a = 5.5732\,\mathring{A}$, $b = 5.5611\,\mathring{A}$, $c = 8.4714\,\mathring{A}$.

IR	Atom	BV components			Magnetic Intensity			
		m_a	m_b	m_c	$(h\,0\,\frac{l}{2})$		$(0\,k\,\frac{l}{2})$	
					$\pi \to \sigma$	$\pi \to \pi$	$\pi \to \sigma$	$\pi \to \pi$
Γ_1	1	1	0	0	Yes	No	No	Yes
	2	-1	0	0				
Γ_2	1	0	1	0	No	Yes	Yes	No
	2	0	1	0				
Γ_4	1	0	0	1	Yes	No	Yes	No
	2	0	0	1				
Γ_5	1	0	0	1	Yes	No	Yes	No
	2	0	0	-1				
Γ_7	1	0	1	0	No	Yes	Yes	No
	2	0	-1	0				
Γ_8	1	1	0	0	Yes	No	No	Yes
	2	1	0	0				

agrees with the observed intensity, we conclude that the magnetic Sm moments are arranged according to the MR Γ_5. Using the Q dependence of the non-resonant scattering, the magnetic structure of the Fe moments can be determined as well. A combined magnetic structure is shown in Fig. 15 (b).

Full polarization analysis using Stokes parameters:

Here we will discuss, how to use linear polarization analysis to determine the moment direction. There are several advantages of using Stokes parameter formalism over the conventional azimuthal scan to determine the moment direction. During the azimuthal scan the sample is rotated and during this rotation the beam can illuminate different parts of the sample if the sample is not precisely centered as it is often the case. For a multi-grain sample, this can increase the systematic error in the measured intensity as a function of azimuth angle. For a commensurate magnetic structure with the presence of multiple charge scattering, in principle, one has to minimize multiple charge scattering at each values of azimuth angle. This procedure might be time consuming. In contrast, one can obtain the same information by changing the incident polarization. The beam is fixed on the sample, and hence the previous problems can be easily avoided. Here we will outline the procedure for full polarization analysis used for the multiferroic compound $TbMn_2O_5$.

$TbMn_2O_5$ is a well known multiferroic where ferroelectric and magnetic order occurs in the same phase. In this compound a complete reversal of ferroelctric polarization has been observed in a small applied magnetic field (~2 T). [39] The mechanism driving multiferroicity in this compound is not fully understood. From several studies, it is clear that rare-earth plays an important role in the magnetoelectric coupling. It was not possible to refine the magnetic struc-

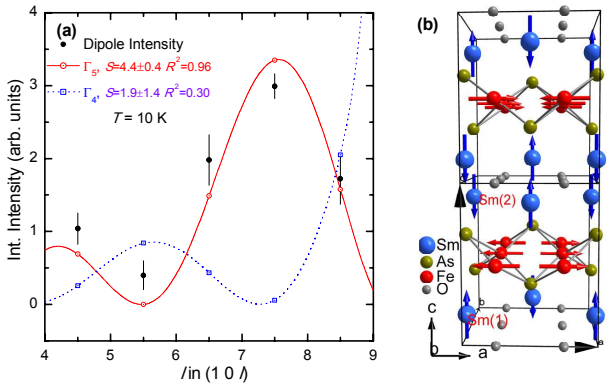

Figure 15: *(a) l dependence of the integrated intensity at the Sm L_2 edge along with the fits for the (1 0 $\frac{l}{2}$) reflections. Open symbols are the calculated intensities. Lines serve as guides to the eye. (b) Proposed magnetic structure in the temperature range 5 K $\leq$ T $\leq$ 110 K. Figure taken from Ref. [34].*

ture of Tb moments in this compound due to a very large no of free parameters in the neutron scattering refinement and the presence of another dominant magnetic subsystem, namely Mn. Resonant magnetic scattering offers an alternative to to study magnetism of Tb moments alone due it's elemental specificity.

$TbMn_2O_5$ shows a series of magnetic transitions. At T_N = 43 K, the manganese moments orders in an incommensurate structure with magnetic propagation vector (δ, 0, τ) with $\delta \approx 0.5$ and $\tau \approx 0.3$. At a slightly lower temperature, T_{FE} =38 K, the system enters into a ferroelectric phase with ferroelectric polarization along the *b* direction. Between $33 \geq T \geq 24$ K, the system locks into a commensurate phase with $\delta = 0.5$ and $\tau = 0.32$. [40, 41] From a full polarization analysis Johnson *et al.* [42] have shown that in the commensurate phase the Tb 5*d* bands are polarized by the manganese subsystem.

A outline to determine the magnetic structure using full polarization analysis will be provided here. At an atomic site (j) the magnetic moment vector can be written as:

$$\vec{m}(j) = m_1\hat{z}_1 + m_2\hat{z}_2 + m_1\hat{z}_3 \tag{32}$$

where m_1, m_2, m_3 are the components of magnetic moment along the directions of $\hat{z}_1$, $\hat{z}_2$, $\hat{z}_3$ respectively (see Fig. 3). The scattering matrix can be calculated for dipole resonance as follows:

$$\begin{aligned} A(\sigma \rightarrow \pi') &= \sum_{j}^{unit-cell} [m_1(j)\cos\theta + m_3(j)\sin\theta]e^{i\vec{q}\cdot\vec{r}_j} \\ &= F(m_1)\cos\theta + G(m_3)\sin\theta \end{aligned} \tag{33}$$

where F and G are two different functions of m_1 and m_3, respectively. In a similar way $\sigma \rightarrow \sigma'$ and $\pi \rightarrow \pi'$ components can be evaluated. Therefore, the scattering matrix can be calculated for dipole resonance can be written as:

$$\begin{aligned} \langle M_m \rangle &= \begin{pmatrix} A_{\sigma\rightarrow\sigma'} & A_{\sigma\rightarrow\pi'} \\ A_{\pi\rightarrow\sigma'} & A_{\pi\rightarrow\pi'} \end{pmatrix} \\ &= \begin{pmatrix} 0 & F(m_1)\cos\theta + G(m_3)\sin\theta \\ -F(m_1)\cos\theta + G(m_3)\sin\theta & L(m_2)\sin 2\theta \end{pmatrix} \end{aligned} \tag{34}$$

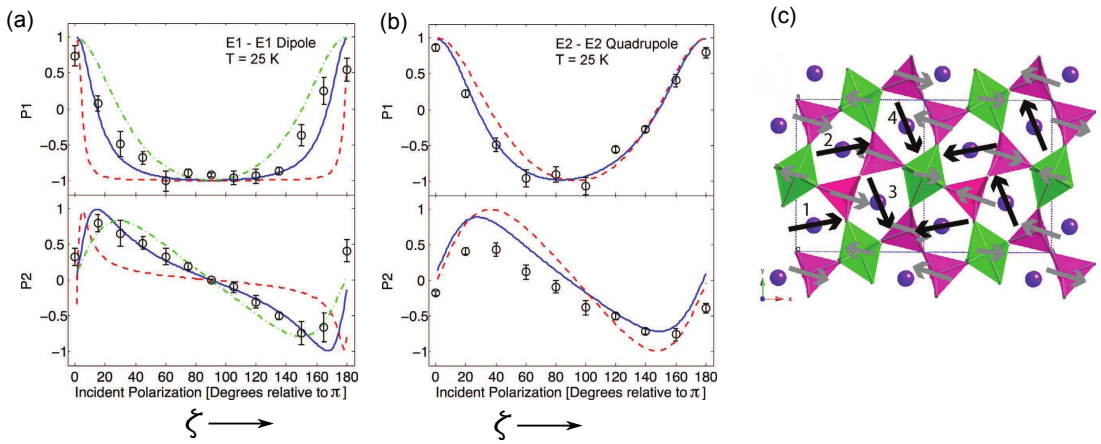

Figure 16: *(a) A plot of the measured Poincaré-Stokes parameters P1 and P2 as a function of the incident x-ray polarization of the commensurate reflection (4+δ, 4, 0-τ) at the E1-E1 (dipole) energy resonance at 25 K. Simulations of the Mn^{4+} and Mn^{3+} magnetic structures as refined by Blake et al. [Ref. [41]] are shown as blue solid and red dashed lines, respectively. A simulation of the terbium magnetic structure scattering at the E1-E1 transition in this phase, as refined in Fig. (b) at the E2-E2 transition, is shown by the green dash-dotted line. (b) A plot of the measured Poincaré-Stokes parameters P1 and P2 as a function of incident x-ray polarization of the commensurate (4+δ, 4, 0-τ) reflection at the E2-E2 (quadrupole) energy resonance at 25 K. (c) Diagrammatic illustration of the refined terbium ion magnetic-moment directions (black arrows) in a the CM phase. Figures taken from Ref. [42] .*

where $L(m_2)$ is a different function of θ. The density matrix of incident linear polarized light with a rotation ζ can be written as:

$$\rho = \frac{1}{2}\begin{pmatrix} 1+\cos 2\zeta & \sin 2\zeta \\ \sin 2\zeta & 1-\cos 2\zeta \end{pmatrix} \tag{35}$$

The final polarization of the scattered beam from the sample can be calculated as follows

$$P_1' = \frac{tr(\sigma_1\rho')}{tr(\rho')} = f(m_1, m_2, m_3, \zeta) \tag{36}$$

$$P_2' = \frac{tr(\sigma_2\rho')}{tr(\rho')} = g(m_1, m_2, m_3, \zeta) \tag{37}$$

where $\rho' = M\rho M^{\dagger}$. P_1' and P_2' can be measured experimentally using a linear polarization analyzer for a particular magnetic reflection as function of ζ and can be refined simultaneously with equation 36 and 37 to obtain the values of the three magnetic moment components. For $TbMn_2O_5$, P_1' and P_2' were measured using a Au(2 2 2) analyzer crystal (see the procedure mentioned in section 4.4) for the commensurate (4+δ, 4, 0-τ) reflection at the dipole and the quadrupole resonance at the Tb L_{III} absorption edge and is shown in Fig. 16(a) and (b) respectively.

Here we recall that the dipole resonance is sensitive to the polarization of the 5*d* band whereas sensitivity to 4*f* magnetism comes from the quadrupole resonance. Fig. 16(a) shows three simulations: (1) The solid blue line is the simulation assuming that the Tb moments are arranged according to the AFM superexchange interaction with nearest Mn^{4+} moments.[43] (2) The red dashed line is the simulation assuming the interaction between Tb and Mn^{3+} moments and (3) the green dashed line is the simulation according to the interaction with the Tb 4*f* moments,

the direction of which is refined in Fig. 16(b). This clearly established that the Tb 5*d* band are polarized by the close proximity of the Mn^{4+}spin density wave, as opposed to Mn^{3+} spin density wave. A reduced χ^2 value of 2.8 of the Mn^{4+} simulation, when compared to the value of 5.8 of the Tb 4*f* band simulation also shows that the Tb 5*d* band is predominantly polarized by the Mn^{4+} 3d band; however, one clearly cannot exclude the interaction with the terbium 4*f* spin configuration.
The magnetic moment direction of the Tb moments was also refined from Fig. 16(b) with moment directions on the 1 and 2 sites were refined to be $10.5\pm2.6^\circ$ in the *a*-*b* plane relative to the *a*-axis and $0.2\pm0.1^\circ$out of the plane and on the Tb 3 and 4 sites $292.5\pm2.0^\circ$in the *a*-*b* plane relative to the *a*-axis and $0.2\pm0.1^\circ$ out of the plane (see Fig.16(c)).
Here we note that the resonant scattering is not only element specific but also band selective. In this case, the Tb 4*f* and 5*d* bands were separately probed by tuning the x-ray energy to the quadrupole and dipole resonances, respectively. The full polarization analysis provides only the moment directions. To determine the absolute value of the magnetic moment, comparison of the nonresonant magnetic intensity with charge intensity is needed and was not performed in this case. One disadvantage of using phase plate is that the incident flux is reduced by at least a factor of ten due to absorption in the diamond crystal. Therefore, it is difficult to do full polarization analysis for small magnetic moment system where the magnetic scattering signal is small.

5.2 Separation of the spin and orbital angular momentum:

We have already discussed during the formulation of nonresonant magnetic scattering cross-section that it is possible to separate spin and orbital angular momentum component using specific polarization properties of the cross section. Here we will discuss the results of Ref. [44] in light of the separation of spin and orbital angular momentum although there exist many other examples [10, 45, 46]. Monooxides of 3*d* transition metals such as MnO, FeO, CoO and NiO are the test samples for the band theory models due to it's simplistic crystal and magnetic structures. Their insulating behavior contradicts simple electronic band models in which the oxygen *p* states are fully occupied while the metal *s* states are empty and the metal *d* states are partially occupied. To resolve this contradiction, two explanations have been proposed: the Mott-insulator concept [47] and band calculations based on local-spin-density approximation that take into account the antiferromagnetic order.[48] The latter approach implies that orbital moment plays a role in CoO and FeO, while such a contribution is not required in NiO. [49] Therefore, the determination of the orbital-moment contribution to the magnetization in the ordered state of NiO is a valuable piece of information towards a better understanding of the electronic and magnetic properties of these compounds.
NiO has the NaCl fcc structure with a = 4.177 Å at room temperature. The ground-state configuration of the Ni^{2+} ion has a $3d^8$ configuration. Below T_N =523 K, NiO orders in the type-II antiferromagnetic structure [50] where ferromagnetic planes are stacked antiferromagnetically along the [1 1 1] axes with their magnetic moments aligned in the [1 1 1] planes along one of the [1 1 $\overline{2}$] directions [51] . The experiment was performed at the ID20 magnetic scattering beamline at the ESRF. The sample was mounted on a four circle diffractometer. A [1 1 1]-axis normal to the surface was carefully oriented along the Φ axis of the four-circle diffractometer. The nonresonant scattering was measured at E = 7.84 keV to match the $2\theta_p$= 90°of the PG(0 0 6) analyzer crystal. The magnetic signal was measured at both the $\sigma \rightarrow \sigma'$ and $\sigma \rightarrow \pi'$ channels. Before, going into details, it is worth to discuss the magnetic domains present in the crystal.

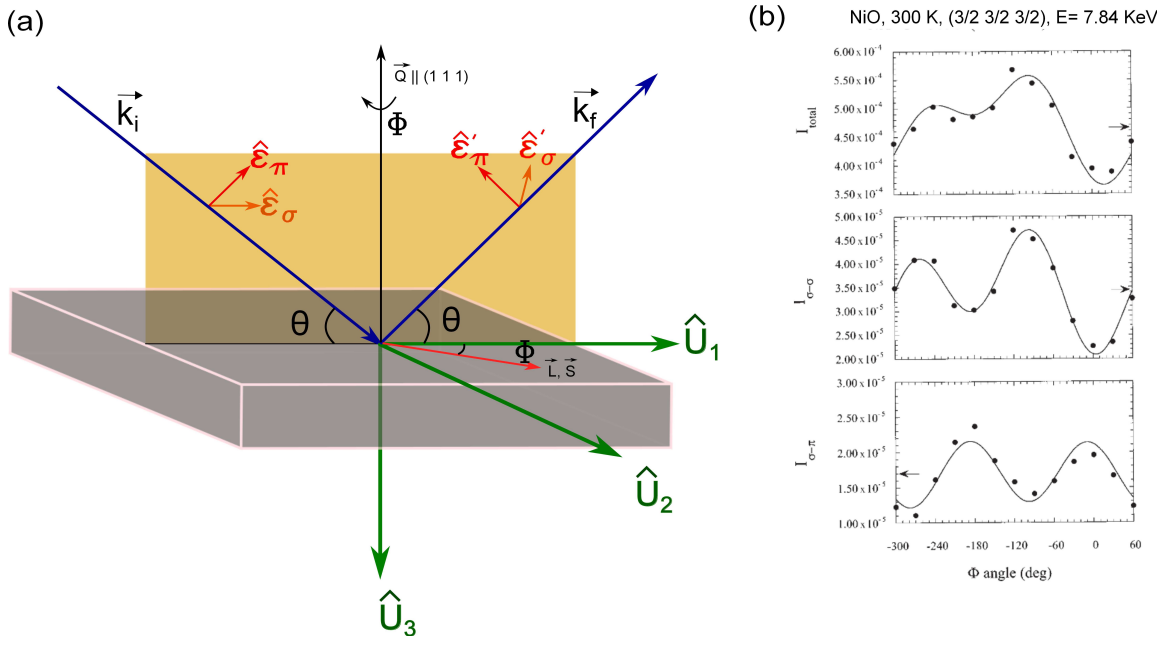

Figure 17: *(a) The scattering geometry for the NiO experiment. (b) Normalized integrated intensities of the* $(\frac{3}{2}\ \frac{3}{2}\ \frac{3}{2})$ *reflection as a function of azimuth angle* Φ *at 7.84 keV. Intensities are given in (radians*detector counts/monitor counts). Errors bars are smaller than the dot size. The two polarized components,* $I_{\sigma\sigma'}$ *and* $I_{\pi\pi'}$*, are out of phase by* $\frac{\pi}{2}$*. The total intensity is the sum of the two components corrected for the reflectivity of the PG(006) analyzer. Arrows indicate the* Φ *averaged values that are used to extract* $L(\vec{Q})$ *and* $S(\vec{Q})$*.*

When the system is cooled from the paramagnetic cubic phase to orthorhombic AFM phase, there exist 4 symmetry equivalent *K* domains. The propagation vector $(\frac{1}{2}, \frac{1}{2}, \frac{1}{2})$ can align in any of the 4 symmetry equivalent directions [1 1 1], [$\bar{1}$ 1 1], [1 $\bar{1}$ 1], [1 1 $\bar{1}$] and give rise to four *K* domains. In addition, the magnetic moments are aligned in the [1 1 1] planes along one of the [1 1 2] directions. Since in the cubic state, the [1 1 1] axis is a three-fold symmetry axis, there exist three equivalent possible spin directions perpendicular to the [1 1 1] axis, the so-called *S*-domains. Depending on crystal faults (surfaces, small angle grain boundaries, impurity atoms etc.), but also on random processes, an arrangement of these *K*- and *S*-domains develops in the sample in the low temperature phase. During the experiment it appears that the sample is populated by a single *K* domain with propagation vector parallel to the surface normal, at least in the near-surface region of 40 μm probed with 7.84 keV x-rays. When measuring the scattering intensities from a given *K* domain, all contributions from the associated *S* domains add incoherently. By rotating the sample about the surface normal (angle Φ in Fig. 17 (a)), we could study the *S* domain distribution within the [1 1 1] *K* domain. Figure 17 (b) shows the Φ dependence of $I_{\sigma\sigma'}$ and $I_{\pi\pi'}$ at the $(\frac{3}{2}\ \frac{3}{2}\ \frac{3}{2})$ position. The two intensities exhibit a modulation of period π characteristic of the *S*-domain distribution. A modulation with a period 2π would indicate that the footprint of the beam is moving across the surface of the sample during the Φ rotation. In a given *S* domain, the magnetic scattering amplitudes vary in a simple manner with the Φ angle: From the non resonant magnetic scattering cross-section we can write:

$$M(\sigma \rightarrow \sigma') = \sin(2\theta)S_2 = \sin(2\theta)\sin\Phi S(\vec{Q}) \quad (38)$$

$$M(\sigma \rightarrow \pi') = -\sin(2\theta)\sin\theta[L_1 + S_1] \quad (39)$$

$$= -\sin(2\theta)\sin\theta[\cos\Phi S(\vec{Q}) + \cos(\Phi + \Phi_0)L(\vec{Q})] \quad (40)$$

where an angular Φ_0 offset is allowed between *S* and *L*. The origin of Φ is taken with the spin direction in the scattering plane. In a multi-*S*-domain sample, scattered intensities are combinations of $\sin^2\Phi$ and $\cos^2\Phi$. Fig. 17(b) shows that the intensity at the $\sigma \rightarrow \sigma'$ and $\sigma \rightarrow \pi'$ are exactly $\frac{\pi}{2}$ phase shifted implying that Φ_0 = 0 which is in agreement with the collinear arrangement of the spin and orbital angular momentum. Taking the ratio of intensities ($I \propto M^2$) using Eqs. 38 and 40, in both geometries, the ratio of $\frac{L(\vec{Q})}{2S(\vec{Q})}$ can be easily calculated. By comparing the calculated ratio with the Φ averaged experimental values as shown in Fig. 17 (b), $\frac{L(\vec{Q})}{2S(\vec{Q})}$ can be determined. $\frac{L(\vec{Q})}{2S(\vec{Q})}$ as a function of $\vec{Q}$ for three different reflections $(\frac{1}{2}\frac{1}{2}\frac{1}{2})$, $(\frac{3}{2}\frac{3}{2}\frac{3}{2})$, $(\frac{5}{2}\frac{5}{2}\frac{5}{2})$ is shown in Fig. 18(a). The results in Fig. 18 clearly show that a large contribution ($17 \pm 3\%$) to the magnetization from the orbital moment exists in NiO. The increase of $L(\vec{Q})/2S(\vec{Q})$ with the scattering vector reflects the broader spatial extent of the spin density. The orbital contribution enhances the spin-alone magnetic moment to make the total moment eventually larger than 2 μ_B as expected for spin-only magnetic moment (S = 1).

The orbital and spin angular momentum can be put in an absolute scale by comparing scattered magnetic intensities with charge intensities and by talking care of extinction correction, if any. The resulting values are shown in Fig. 18(b) as a function of the scattering vector. The extrapolated values at zero scattering vector, $S(0) = 0.95 \pm 0.1$ and $L(0) = 0.32 \pm 0.05$, lead to a value of $2.2 \pm 0.2 \mu_B$ for the staggered magnetization at T = 300 K. This is in close agreement with neutron results giving 1.81 ± 0.2 μ_B [52] and 1.97 μ_B [53].

Summarizing the main results of NiO, (a) the spin and orbital contributing to the total magnetization was measured using nonresonant magnetic scattering. The extrapolation at $\vec{Q}$ = 0 shows that the effective *L*/*S* ratio amounts to 0.34. This is unexpectedly large contribution in transition metal oxides like NiO where *L* is supposed to be largely quenched. Furthermore the orbital angular momentum is parallel to spin, as expected from simple spin-orbit coupling for a $3d^8$ free atom. The results also indicate a contraction of the atomic wave function for Ni in NiO, if the experimental values are compared with the predictions of theory. The atomic wave functions are contracted by 17 % as compared to the free ion. We can conclude that the magnetization density in a simple system like NiO is not yet fully understood and the results of these studies have to be taken into account, when models for the electronic and magnetic structure and properties of transition metal compounds are being made.

5.3 Nonresonant magnetic scattering from Ho Metal:

Nonresonant magnetic scattering from Ho metal illustrates the advantages of magnetic x-ray scattering compared to the neutron scattering and reveals new features in magnetic structure that was unobserved in neutron diffraction experiments [4, 56, 57]. Ho metal has an h.c.p. crystal structure with two layers per chemical unit cell and a large magnetic moment of $10\mu_B$/atom. Below the magnetic ordering temperature, $T_N \approx$ 131K, a pair of satellite reflection appears around each main Bragg reflection parallel to the reciprocal *c* axis [57, 58]. These results are usually taken as evidence for a simple spiral antiferromagnetic structure in which the average

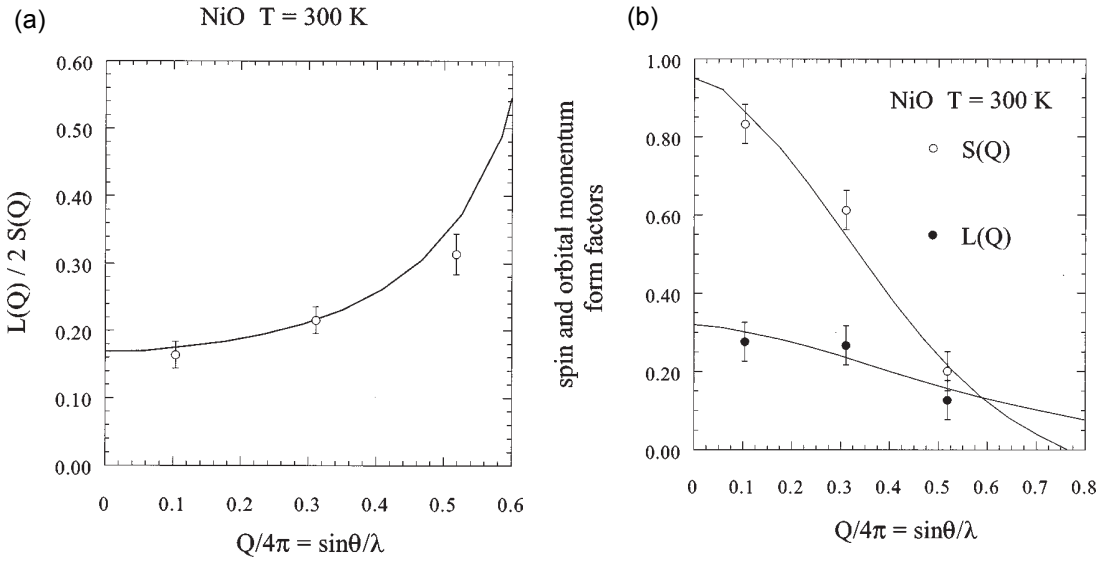

Figure 18: *(a) Measured variation of* $L(\vec{Q})/2S(\vec{Q})$ *as a function of* $\sin\frac{\theta}{\lambda} = \frac{Q}{4\pi}$. *The continuous line is the K dependence estimated by Blume [Ref. [54]] adjusted to fit through the data with a contraction of the wave function by 17%.* $L(\vec{Q})/2S(\vec{Q})$ *extrapolates to 0.17 at* $\vec{Q} = 0$. *(b) Spin form factor and orbital-moment form factor in NiO. The data have been obtained by normalizing magnetic intensities to charge peaks corrected for extinction. The continuous lines are the calculated variations of* $S(\vec{Q})$ *and* $L(\vec{Q})$ *with* $\sin\frac{\theta}{\lambda}$ *from Refs. [54] and [55] with an expansion of the* $\vec{Q}$ *scale by 17%.*

moments are aligned ferromagnetically within the basal planes, but rotate from one plane to the next plane with an average turn angle varying between ≈50°/layer at T_N and ≈30°/layer near T_c. The exact turn angle can be determined by measuring the modulation wave vector at each temperature. Figure 19 shows the schematic of the magnetic structure along with the temperature dependence of the magnetic propagation vector.

Gibbs *et al.* [4] first reported non-resonant x-ray magnetic scattering on Ho. The count rate of the magnetic signal was comparable with neutron diffraction (~25 counts/sec). The background of the NRXMS was one order of magnitude higher than that of neutron. This was more than compensated for by a five fold increase of resolution, which proved to be very important for the success of the experiment. The wave-vector resolution of 10^{-3} Å^{-1} reveals new features in the temperature dependence of the propagation vector and leads to a new model of the magnetic structure. The temperature dependence of the propagation vector measured by x-rays is in very good agreement with the neutrons as is shown in Fig. 19(a). In addition, several lock-in transition was observed as shown in the inset of Fig. 19(a). Below 50 K thermal hysteresis, irreversibility, coexistence of phases with differing wave vector, and apparent lock-in behavior was observed.

Figure 20 (a) shows the diffraction pattern obtained with synchrotron radiation at 17 K when the magnetic satellite is located at a commensurate position $\tau_m = \frac{5}{27}$. A second peak of intensity comparable with the satellite but of greater width (0.0075 vs 0.005 Å^{-1}) is observed at $\tau_c = \frac{2}{9}$. As the temperature is increased, τ_m shifts away from $\frac{5}{27}$, and the second peak apparently broadens and disappears. To establish the origin of the additional scattering at $\frac{2}{9}$, the scan at 17 K was repeated with the polarization analyzer in place. As seen in Fig. 20(a), the second peak is completely eliminated when measured with PG(0 0 6) analyzer crystal in the $\sigma \rightarrow \pi'$

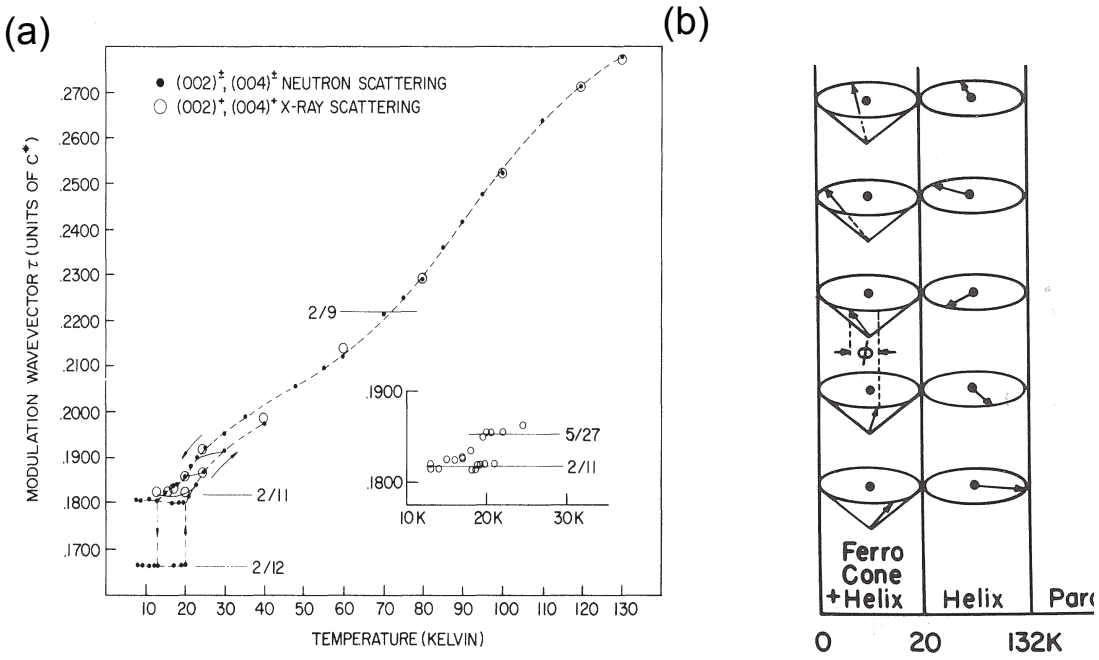

Figure 19: *(a) Temperature dependence of the Ho modulation wave vector τ obtained with both synchrotron x-ray (open circles) and neutron (filled circles) scattering. The wave vectors obtained by neutron scattering in the coexistence region below 20 K are the result of fits to the first harmonic. Th fine lines across the hysteresis loop indicate the results of cycles of the temperature below 50 K. Inset: Plot of the wave vectors obtained from several cycles of the temperature between 13 and 24.5 K obtained with x-ray scattering. [4] (b) Schematic of the magnetic structure of Ho determined using neutron diffraction as a function of temperature. [7].*

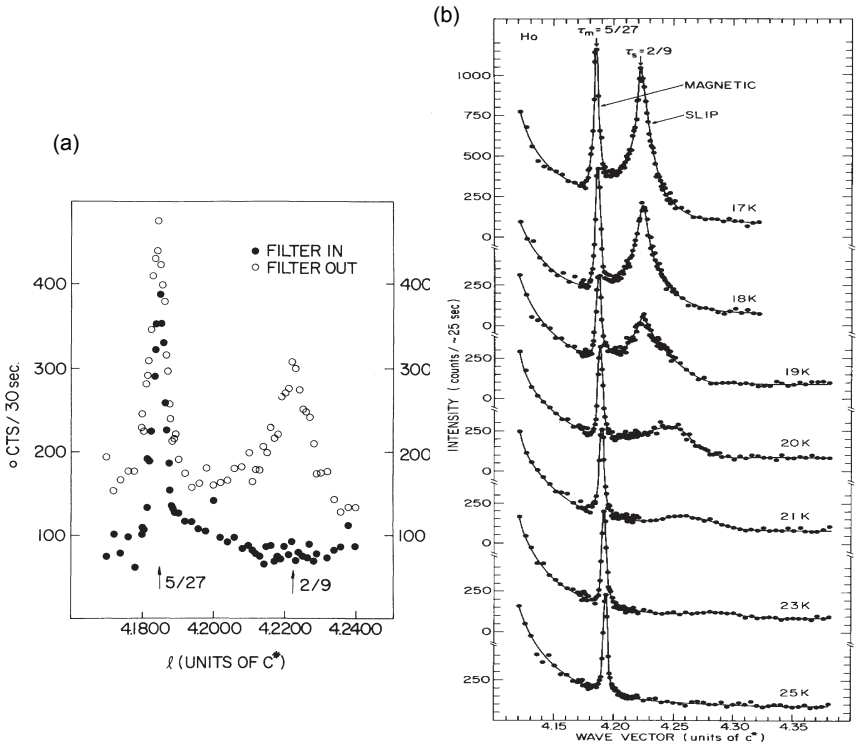

Figure 20: *(a) Open circles: Scan of the Ho(004) magnetic ($\tau = \frac{5}{27}$) and charge ($\tau = \frac{2}{9}$) satellites taken at 17 K. Filled circles: The same scan, but with the polarization analyzer in place.(b) Temperature dependence of the magnetic and charge satellites measured during cooling.[59]*

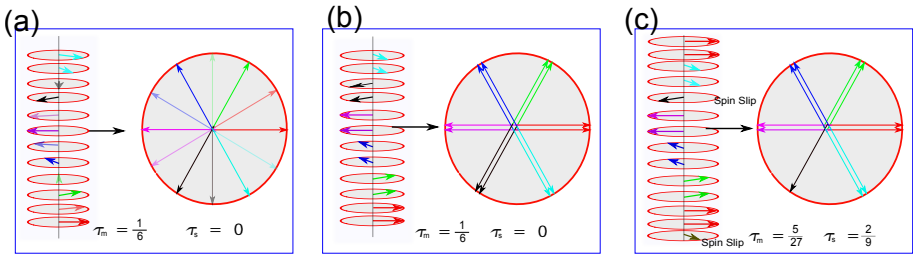

Figure 21: *(a) The magnetic structure proposed by neutron scattering at low temperature where moments in the consecutive layers rotates by 30°. (b) The low temperature magnetic structure as proposed by Gibbs et al. [4] where a pair of doublet rotates by 60° giving the same propagation vector as (a). (c) The spin-slip model for the magnetic structure. In(a)-(c), the right sides depicts projection of the magnetic moments in the hexagonal a-b plane.*

scattering channel, showing unambiguously that (1) the scattering at τ_m=$\frac{5}{27}$, is magnetic in origin, and (2) the peak at τ_c=$\frac{2}{9}$, originates from the charge scattering. For a pure spiral with the propagation vector perpendicular to the moment direction, magnetoelastic coupling is zero and thus, no periodic modulation of the lattice is expected [7]. Therefore, the existence of the charge scattering at $\tau_c = \frac{2}{9}$ is completely unexpected from the previous model of the magnetic structure.

The existence of the commensurate magnetic satellite and associated charge scattering can be explained based on the spin slip model. Spin slip model of the magnetic structure is based on the low temperature τ_m= $\frac{1}{6}$ structure which is schematically shown in the Fig. 21. In this structure the pairs of magnetic moments or doublets are oriented along one of the easy directions of hexagonal lattice. The adjacent pairs are rotated by 60° so that 12 atomic layers or 6 chemical unit cells are needed to complete a 360°turn. Thus the magnetic period τ_m= $\frac{1}{6}$. Shorter period modulations occur due to periodic spin slips where single atomic layer (singlet) makes a 60° turn as shown in Fig. 21(c). In principle, the spin-slip model allows a large number of possible sequences of doublet and singlet, producing modulation wavevector in the range $\frac{1}{3} \geq \tau_m \geq \frac{1}{6}$. The change in magnetoelastic coupling at spin-slip sites causes a small distortion of the chemical lattice, with a period equal to the spin slip period. The spin-slip model describes not only the lock-in behavior of the magnetic modulation wave vector, but also predicts also the wave vector for the charge scattering. In Ho it was proposed that the magnetic structure consists of two basic blocks: the spin-slip block consisting of single atomic layer and a no-spin-slip block consisting of a doublet. A magnetic unit cell then can be described as a sequence of *N* no-slip blocks and *S* spin-slip blocks. For the periodic sequence of *N* ans *S* blocks it can be shown in the case of Ho metal that: [7]

$$\tau_m = \frac{m+1}{6m+3} \tag{41}$$

$$\tau_c = \frac{2}{2m+1} \tag{42}$$

where $m = \frac{N}{S}$. Some of the allowed wave-vectors for different values of *m* are given in Table 4. One can see that there is a remarkable agreement between the allowed wave-vectors in the spin-slip model and the observed experimental data shown in Fig. 19(a). Although we have assumed a periodic structure for the spin-slip array, it is clear from the data of Fig. 20 that the peak at $\frac{2}{9}$ is not instrumentally narrow. This width is direct evidence of the lack of long range periodicity in the spin-slip distribution.

Table 4: *Some of the commensurate magnetic (τ_m) and lattice modulation wave vectors predicted by the spin-slip model of Ho [7]. The rotation of magnetic moment between no-spin-slip block and spin-slip block is 60°.*

m	0	1	2	3	4	5	6	∞
τ_m	$\frac{1}{3}$	$\frac{2}{9}$	$\frac{1}{5}$	$\frac{4}{21}$	$\frac{5}{27}$	$\frac{2}{11}$	$\frac{7}{39}$	$\frac{1}{6}$
τ_s	2	$\frac{2}{3}$	$\frac{2}{5}$	$\frac{2}{7}$	$\frac{2}{9}$	$\frac{2}{11}$	$\frac{2}{13}$	0

So far we have discussed nonresonant magnetic diffraction at low to medium energies (4-20 keV). The nonresonant magnetic diffraction can be performed also at very high energies which has several advantages. First of all, instead of specialized Be windows, less expensive Aluminum windows can be used due to less absorption at high energies. Secondly, due to the high

penetration of the high energy x-rays, bulk sample can be probed in transmission geometry and one do not have to worry about sample surface preparation. For 3*d* transition metals, the absorption length increases from some μm at 8 keV to several mm at 80 keV. Due to the enhancement of penetration depth, the effective scattering volume increases and hence, the scattering intensity increases by a factor of 3-4 orders of magnitude. Corrections for absorption, extinction, beam foot print etc. are simple and therefore, by normalizing the intensity of the magnetic reflections to the intensity of the charge reflections, absolute values for the spin moment can be determined [60]. For high energies, scattering angles are very small for the low index reflections. Therefore, neglecting terms in $\sin^2\theta$ one can write the nonresonant magnetic cross-section as follows:

$$\begin{aligned} \langle M_m \rangle &= \begin{pmatrix} A_{\sigma\to\sigma'} & A_{\sigma\to\pi'} \\ A_{\pi\to\sigma'} & A_{\pi\to\pi'} \end{pmatrix} \\ &= \begin{pmatrix} (\sin 2\theta)S_2 & -0 \\ 0 & (\sin 2\theta)S_2 \end{pmatrix} \end{aligned} \tag{43}$$

We can see from the matrix Eq. 43 that the magnetic scattering at high energies is only sensitive to spin component perpendicular to the scattering plane and the scattering does not change the polarization state. Nonresonant magnetic scattering at high energies has been successfully employed to study the magnetism of MnF_2 by Strempfer *et al.* [61]. With 80 keV x-rays a high peak count rates 13000 counts/sec with a peak to background ratio of 230:1 and a very high reciprocal space resolution can be obtained for the magnetic (3 0 0) reflection as shown in Fig. 22(a). Figure 22 (b) shows a measurement of the temperature dependence of the sublattice magnetization. In the critical region close to the Neél temperature T_N, the reduced sublattice magnetization $m = M(T)/M(T=0)$ follows very accurately a power law behavior:

$$m(\tau) = D\tau^{\beta} \tag{44}$$

as a function of the reduced temperature $\tau = (T_N - T)/T_N$. The value of the critical exponent of β = 0.333(3) corresponds well to the predictions of the Ising model. As discussed previously, the problem of multiple charge scattering is severe at high energies and unfortunately, it was the case for MnF_2 due to the identical chemical and magnetic unit cell and specific crystal symmetry. Multiple charge scattering was minimized by judiciously selecting the azimuth angle as discussed in section 5.1.1.

5.4 Magnetic scattering from ferromagnet:

We have discussed applications of resonant and nonresonant magnetic scattering in the case of antiferromagnets where magnetic signal is well separated form charge scattering. For a ferromagnetic samples or in an atiferromagnets with $\vec{Q}$ = 0, where charge and magnetic scattering coincide, it seems impossible to measure the magnetic signal. However, it has been shown that for a ferromagnet it is possible to measure magnetic signal by measuring (a) flipping ratio (asymmetry ratio) in a magnetic field or (b) by using the the fact that the charge scattering from a sample is suppressed by a factor of $\cos^2 2\theta_{sample}$ in addition to $\cos^2 2\theta_{analyzer}$ in $\pi \to \sigma'$ scattering geometry.

(a) The total scattering cross-section generated by the magnetic and charge scattering length is:[7]

$$\frac{d\sigma}{d\omega} = |f|^2 = |f_m + f_c|^2 \tag{45}$$

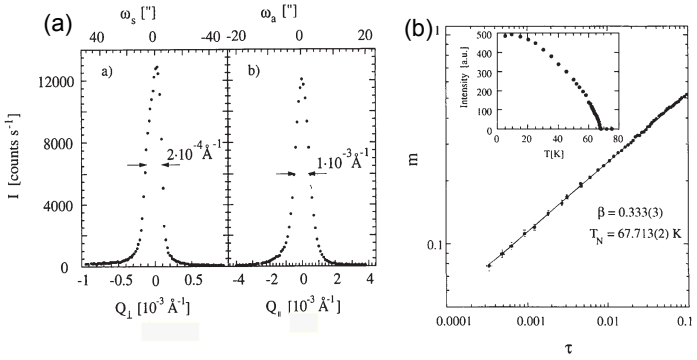

Figure 22: *(a) Representative scans of the magnetic (3 0 0) reflection at T = 5 K. (a) and (c) show transversal scans in the three and two crystal modes, respectively.(b)The main graph shows the reduced magnetization* m=M(T)/M(0) *as a function of the reduced temperture* $\tau = (T_N - T)/T_N$ *on a double logarithmic scale for the magnetic (3 0 0) reflection. The points are taken from the measurement, the solid line represents a fit using equation 44. The inset shows the temperature dependence of the intensity of the magnetic (3 0 0) reflection from 5 to 80 K with* T_N *= 67.713 K. Figure adapted from Ref. [61].*

If f_m and f_c are exactly in phase, then the Eq. 45 can be written as:

$$\frac{d\sigma}{d\omega} = f_c^2 + f_m^2 + 2f_c f_m \tag{46}$$

Eq.46 has three terms: the first term is the pure charge scattering which is the most dominant term. The second term is the pure magnetic term and the third term is due to the interference between charge and magnetic signals. The pure magnetic term is 10^{-6} times weaker than the pure charge term and therefore, undetectable in a magnetic scattering experiment. The third term being linear in f_m, it is much stronger than the pure magnetic term. Moreover, being linear in f_m, the sign of the third term can be changed by changing the magnetization direction by an external magnetic field. Thus, the difference in the cross section for two different orientation of the magnetic field can be detected.

Unfortunately, in a centrosymmetric crystal structure, the f_m and f_c are exactly out of phase for the plane polarized incident light, and therefore, the interference term vanishes. The interference term for the centrosymmetric case only exists if the incident light is elliptically polarized. In a non-centrosymmetric crystal structure the scattering phases depend on the precise distribution of the charges and magnetic moment in the unit cell and depending on the phase difference an interference term is permitted. One clever way to introduce a phase difference is to tune the x-ray energy to the absorption edge of one of the element in the crystal. Resonant scattering introduces a strong energy dependent phase shift and hence an interference term is allowed. Charge magnetic interference was first seen in ferromagnetic Ni single crystal at the Ni *K* edge. By reversing the direction of external magnetic field applied perpendicular to the horizontal scattering plane an asymmetry ratio can be calculated:

$$R_a = \frac{I\uparrow - I\downarrow}{I\uparrow + I\downarrow} \tag{47}$$

Where $I\uparrow$ and $I\downarrow$ represent scattering intensities for two opposite magnetization direction. The value of asymmetry ratio R_a of 10^{-3} and 0.1 was reported for Ni [62]and CoPt alloy [63],

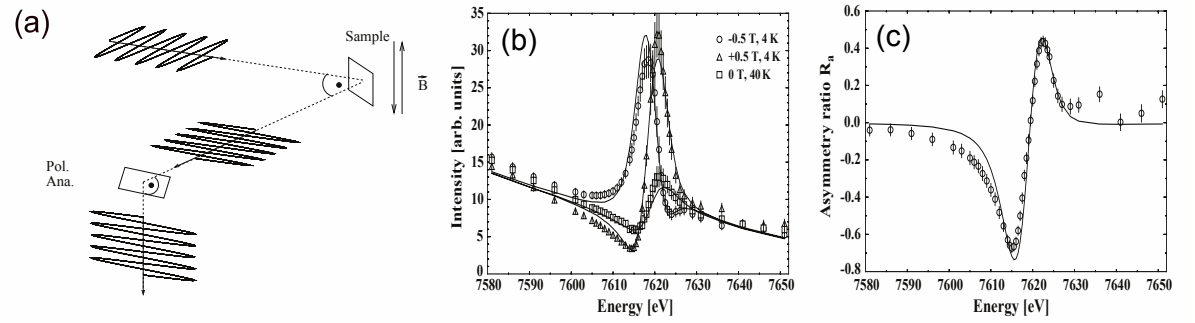

Figure 23: *(a) Experimental set-up for the measurement of XRMS from ferromagnetic samples. The primary beam is polarized horizontally, the magnetic field is applied perpendicular to the horizontal scattering plane. The Bragg peak of the sample and the analyzer were chosen to scatter close to 90 degrees to minimize the charge scattering. (b) Absorption-corrected energy dependence of the (1 1 5) reflection measured at the Eu* L_{II} *edge. Two measurements with magnetic fields of +0.5 T and −0.5 T were performed at 4 K. Charge and magnetic intensities contribute to the scattering amplitude. (c) Asymmetry ratio* R_a *of the (1 1 5) reflection at 4 K at the Eu* L_{II} *edge. Figures adapted from Ref. [64].*

respectively. The asymmetry ratio was also measured at the Eu L_{II} edge for the EuS single crystal and the ratio as large as R_a of 0.67 was obtained [64].
Fig. 23 (a) shows the experimental geometry for measuring the flipping ratio for the EuS single crystal. The (1 1 5) reflation was measured in the $\pi \rightarrow \pi'$ scattering geometry to suppress charge signal relative to the magnetic scattering signal and to access the magnetic moment component perpendicular to the scattering plane. In the $\pi \rightarrow \pi'$ scattering geometry, resonant scattering amplitude is sensitive to the magnetic moment perpendicular to the scattering plane i.e. in the direction of the applied magnetic field (m_z). Therefore, we can write:

$$I = I_{mag} \left\langle m_z^2 \right\rangle + I_{int} \left\langle m_z \right\rangle + I_{charge}$$

where I_{mag} is the pure magnetic term, I_{charge} is the charge term and I_{int} is the interference term and $\langle m_z \rangle$ is the expectation value of the magnetic moment along the field direction. Figure 23(b) shows the resonance spectra at the Eu L_{II} edge below and above the ferromagnetic transition temperature of 17 K. The resonance spectra below T_c was measured for two opposite field directions. The asymmetry ratio can be calculated using the formula 47 and is shown in Fig. 23 (c). Clearly the asymmetry ratio is quite large compared to Ni and CoPt. Important spectroscopic information such as the exchange splitting of the 5*d* conduction band can be obtained by fitting the scattered intensity on the energy and the applied magnetic field [64]. The exchange splitting was found to be $\epsilon = 0.27(1)$eV.
Ferrimagnetism of Gd moments in $GdNi_2Ge_2$ [65] as well as antiferromagnetism with Q = 0 magnetic structure in SmFeAsO [34] were studied in zero magnetic field using XRMS at the Gd L_{II} and Sm L_{II} edges, respectively. In both cases, the authors employed $\pi \rightarrow \sigma'$ scattering geometries where the charge signal can be reduced by $\cos^2 2\theta_{analyzer} \times \cos^2 2\theta_{sample}$ compared to the reduction by $\cos^2 2\theta_{analyzer}$ in the $\sigma \rightarrow \pi'$ scattering geometry. In the $\pi \rightarrow \sigma'$ scattering geometry with scattering angle of the sample ($2\theta_{sample}$) close to 90° the charge scattering is reduced by a factor of 10^{-6}. Therefore, the charge and magnetic scattering intensities become comparable and measurement of magnetic signal becomes feasible.

In the above examples, resonant magnetic term interfere with the charge scattering and is known as resonant magnetic-charge interference. Similarly one can utilize the interference term between nonresonant magnetic and resonant charge scattering by tuning the x-ray energy to the absorption edge of a nonmagnetic element in the crystal. This is known as magnetic-resonant charge interference scattering. One can also go far above the absorption edge associated with a weak resonance enhancement (such as *K*-edges of transition metal) so that the resonance enhancement is small and still there is a phase shift which leads to nonzero interference term. This approach was utilized in the first magnetic scattering experiments on ferromagnets [63].

6 Summary

The above examples clearly demonstrates that magnetic x-ray scattering becomes a microscopic probe of magnetism. Like any other experimental techniques magnetic x-ray scattering has it's own weaknesses and strengths. For example, determination of a completely unknown magnetic structure is very difficult since magnetic signal from powder sample is very weak compared to the charge signal. Therefore, magnetic structure determination from powder samples will remain a typical task for neutron scattering where nuclear and magnetic signal have comparable intensities. It is also very difficult to determine the absolute value of the ordered magnetic moment using nonresonant x-ray scattering. Nevertheless, using nonresonant x-ray magnetic scattering, it is possible to separate spin and orbital angular momentum which is not possible using neutron diffraction. Furthermore, in contrast to neutron scattering, resonant scattering is not only element specific but also band selective as shown in the case of $TbMn_2O_5$. Due to the intrinsic collimation of the synchrotron x-rays, the Q-space resolution is much better for a synchrotron experiment. This is often helpful to study incommensurate magnetic structure and detect lock-in transitions as in the case of Ho metal. Magnetic x-ray scattering provides an alternative to study magnetism of compounds which contains strongly neutron absorbing materials such as Gd, Sm,Eu etc. The magnetic form factors for the XRMS, NRXMS and neutron scattering are quite different. In XRMS, the spatial extension of the core levels is relevant and therefore virtually no decrease of the scattering amplitude as a function of momentum transfer is observed. In non-resonant x-ray scattering, the form factors of spin and angular momentum can be determined separately, while neutrons are sensitive to a combination of both.
In summary, both magnetic x-ray and neutron scattering are complementary probe of magnetism and one has to select both methods or any one of them depending on the specific problem.

References

[1] P. M. Platzman and N. Tzoar, Phys. Rev. B **2**, 3556 (1970).

[2] F. D. Bergevin and M. Brunel, Phys. Lett. A **39**, 141 (1972).

[3] F. de Bergevin and M. Brunel, Acta Crystallogr. **A37**, 314 (1981).

[4] D. Gibbs, D. E. Moncton, K. L. D'Amico, J. Bohr, and B. H. Grier, Phys. Rev. Lett. **55**, 234 (1985).

[5] D. Gibbs, D. R. Harshman, E. D. Isaacs, D. B. McWhan, D. Mills, and C. Vettier, Phys. Rev. Lett. **61**, 1241 (1991).

[6] E. Balcar and S. Lovesey, *Theory of magnetic neutron and photon scattering* (Oxford University Press, 1989).

[7] S. Lovesey and S.P.Collins, *X-ray scattering and absorption by magnetic materials* (Oxford Science Publications, 1996).

[8] T. Brückel, lecture notes on "Magnetic X-Ray Scattering".

[9] M. Blume, J. Appl. Phys. **57**, 3615 (1985).

[10] M. Blume and D. Gibbs, Phys. Rev. B **37**, 1779 (1988).

[11] J. P. Hill and D. F. McMorrow, Acta Crystallogr. **A52**, 236 (1996).

[12] J. P. Hannon, G. T. Trammell, M. Blume, and D. Gibbs, Phys. Rev. Lett. **61**, 1245 (1988).

[13] J. W. Kim, Y. Lee, D. Wermeille, B. Sieve, L. Tan, S. L. Bud'ko, S. Law, P. C. Canfield, B. N. Harmon, and A. I. Goldman, Phys. Rev. B **72**, 064403 (2005).

[14] C. Detlefs, A. H. M. Z. Islam, A. I. Goldman, C. Stassis, P. C. Canfield, J. P. Hill, and D. Gibbs, Phys. Rev. B **55**, R680 (1997).

[15] C. Detlefs, Ph.D. thesis, Iowa State University, Ames, Iowa, USA (1997).

[16] M. D. Hamrick, M. A. Thesis, Rice University (1990).

[17] J. P. Hill and D. F. McMorrow, Acta Cryst. **A52**, 236 (1996).

[18] A. I. Goldman, K. Mohanty, G. Shirane, P. M. Horn, R. L. Greene, C. J. Peters, T. R. Thurston, and R. J. Birgeneau, Phys. Rev. B **36**, 5609 (1987).

[19] T. Brückel, M. Lippert, T. Köhler, J. R. Schneider, W. Prandl, V. Rilling, and M. Schilling, Acta Crystallogr. **A52**, 427 (1996).

[20] J. P. Hill, Q. Feng, R. J. Birgeneau, and T. R. Thurston, Z. Phys. B **92**, 285 (1993).

[21] D. Mannix, P. de Camargo, C. Giles, A. de Oliveira, F. Yokaichiya, and C. Vettier, Eur.. Phys. J. B **20**, 19 (2001).

[22] M. K. Sanyal, D. Gibbs, J. Bohr, and M. Wulff, Phys. Rev. B **49**, 1079 (1994).

[23] J. Als-Nielsen and D. McMorrow, *Elements of Modern X-ray Physics* (John Wiley & Sons, New York, 2001).

[24] J. P. Hill, *Magnetic x-ray scattering* (John Wiley & Sons, New York, 2002).

[25] C. Giles, C. Vettier, F. de Bergevin, C. Malgrange, G. Grubel, and F. Grossi, Rev. Sci. Instrum. **66**, 1518 (1995).

[26] L. Bouchenoire, S. D. Brown, P. Thompson, J. A. Duffy, J. W. Taylor, and M. J. Cooper, J. Synchrotron Radiat. **10** (2003).

[27] C. M. C. Detlefs, M. Sanchez del Rio, arXiv:1106.4446 (2011).

[28] V. K. Pecharsky and K. A. Gschneidner, Jr., Phys. Rev. Lett. **78**, 4494 (1997).

[29] V. K. Pecharsky and J. K. A. Gschneidner, Appl. Phys. Lett. **70**, 3299 (1997).

[30] L. Morellon, J. Stankiewicz, B. García-Landa, P. A. Algarabel, and M. R. Ibarra, Appl. Phys. Lett. **73**, 3462 (1998).

[31] L. Morellon, J. Blasco, P. A. Algarabel, and M. R. Ibarra, Phys. Rev. B **62**, 1022 (2000).

[32] L. Tan, A. Kreyssig, J. W. Kim, A. I. Goldman, R. J. McQueeney, D. Wermeille, B. Sieve, T. A. Lograsso, D. L. Schlagel, S. L. Budko, et al., Phys. Rev. B **71**, 214408 (2005).

[33] S.-L. Chang, *Multiple Diffraction of X-Rays in Crystals* (Springer-Verlag, 1984).

[34] S. Nandi, Y. Su, Y. Xiao, S. Price, X. F. Wang, X. H. Chen, J. Herrero-Martin, C. Mazzoli, H. C. Walker, L. Paolasini, et al., Phys. Rev. B **84**, 054419 (2011).

[35] Y. Kamihara, T. Watanabe, M. Hirano, and H. Hosono, J. Am. Chem. Soc. **130**, 3296 (2008).

[36] M. Rotter, M. Tegel, and D. Johrendt, Phys. Rev. Lett. **101**, 107006 (2008).

[37] A. Martinelli, A. Palenzona, C. Ferdeghini, M. Putti, and H. Emerich, J. Alloy. Compd. **477**, L21 (2009).

[38] A. S. Wills, Physica B **276-278**, 680 (2000).

[39] N. Hur, S. Park, P. Sharma, J. Ahn, S. Guha, and S. Cheong, Nature **429**, 392 (2004).

[40] L. C. Chapon, G. R. Blake, M. J. Gutmann, S. Park, N. Hur, P. G. Radaelli, and S.-W. Cheong, Phys. Rev. Lett. **93**, 177402 (2004).

[41] G. R. Blake, L. C. Chapon, P. G. Radaelli, S. Park, N. Hur, S.-W. Cheong, and J. Rodriguez-Carvajal, Phys. Rev. B **71** (2005).

[42] R. D. Johnson, S. R. Bland, C. Mazzoli, T. A. W. Beale, C.-H. Du, C. Detlefs, S. B. Wilkins, and P. D. Hatton, Phys. Rev. B **78**, 104407 (2008).

[43] C. Vecchini, L. C. Chapon, P. J. Brown, T. Chatterji, S. Park, S.-W. Cheong, and P. G. Radaelli, Phys. Rev. B **77**, 134434 (2008).

[44] V. Fernandez, C. Vettier, F. de Bergevin, C. Giles, and W. Neubeck, Phys. Rev. B **57**, 7870 (1998).

[45] L. D. Collins, S. P. and G. H. Guo, J. Phys. Condens. Matter **5**, L637 (1993).

[46] C. S. Laundry, D. and A. J. Rollason, J. Phys. Condens. Matter. **3**, 369 (1991).

[47] B. Brandow, Adv. Phys. **26**, 651 (1977).

[48] K. Terakura, A. R. Williams, T. Oguchi, and J. Kübler, Phys. Rev. Lett. **52**, 1830 (1984).

[49] K. Terakura, T. Oguchi, A. R. Williams, and J. Kübler, Phys. Rev. B **30**, 4734 (1984).

[50] C. G. Shull, W. A. Strauser, and E. O. Wollan, Phys. Rev. **83**, 333 (1951).

[51] J. Baruchel, M. Schlenker, K. Kurosawa, and S. Saito, Philos. Mag. B **43**, 853 (1981).

[52] H. A. Alperin, Phys. Rev. Lett. **6**, 55 (1961).

[53] B. E. F. Fender, A. J. Jacobson, and F. A. Wedgwood, J. Chem. Phys. **48**, 990 (1968).

[54] M. Blume, Phys. Rev. **124**, 96 (1961).

[55] R. E. Watson and A. J. Freeman, Acta Crystallogr. **14**, 27 (1961).

[56] W. C. Koehler, J. W. Cable, H. R. Child, M. K. Wilkinson, and E. O. Wollan, Phys. Rev. **158**, 450 (1967).

[57] W. C. Koehler, J. W. Cable, M. K. Wilkinson, and E. O. Wollan, Phys. Rev. **151**, 414 (1966).

[58] M. J. Pechan and C. Stassis, J. Appl. Phys. **55**, 1900 (1984).

[59] J. Bohr, D. Gibbs, D. Moncton, and K. D'Amico, Physica A **140**, 349 (1986).

[60] J. Strempfer, U. Rütt, and W. Jauch, Phys. Rev. Lett. **86**, 3152 (2001).

[61] J. Strempfer, T. Brückel, U. Rütt, J. R. Schneider, K.-D. Liss, and T. Tschentscher, Acta Crystallogr. **A52**, 438 (1996).

[62] K. Namikawa, M. Ando, T. Nakajima, and H. Kawata, J. Phys. Soc. Jpn. **54**, 4099 (1985).

[63] F. de Bergevin, M. Brunel, R. M. Galera, C. Vettier, E. Elkaim, M. Bessiere, and S. Lefebvre, Phys. Rev. B **46**, 10772 (1992).

[64] D. Hupfeld, O. H. Seeck, J. Voigt, J. Bos, K. Fischer, and T. Brückel, Europhys. Lett. **59**, 284 (2002).

[65] J. W. Kim, A. Kreyssig, P. Ryan, E. Mun, P. C. Canfield, and A. I. Goldman, Appl. Phys. Lett. **90**, 202501 (2007).